Experiments in Fluids (2023) 64:185
https://doi.org/10.1007/s00348-023-03721-9

RESEARCH ARTICLE

Homogeneous turbulence in a random-jet-stirred tank

Joo Young Bang[1] · **Nimish Pujara**[1]

Received: 1 June 2023 / Revised: 12 September 2023 / Accepted: 1 October 2023

Abstract

We report an investigation into random-jet-stirred homogeneous turbulence generated in a vertical octagonal prism-shaped tank where there are jet arrays on four of the eight vertical faces. We show that the turbulence is homogeneous at all scales in the central region of the tank that span multiple integral scales in all directions. The jet forcing from four sides in the horizontal direction guarantees isotropy in horizontal planes but leads to more energy in the horizontal fluctuations compared with the vertical fluctuations. This anisotropy between the horizontal and vertical fluctuations decreases at smaller scales, so that the inertial and dissipation range statistics show isotropic behavior. Using four jet arrays allows us to achieve higher turbulence intensity and Reynolds number with a shorter jet merging distance compared to previous facilities with two-facing arrays. By changing the array-to-array distance, the parameters of the algorithm that drives random-jet stirring, and attachments to the exits of each jet, we show that we are able to vary the turbulence scales and Reynolds number. We provide scaling relations for the turbulent fluctuation velocity, integral scale, and dissipation rate, and we show how these scales of motion are primarily determined by the properties of individual jets and the diffusion of their momentum with distance from the nozzles. Finally, we examine the signatures of individual jets in the turbulent velocity spectra and report the conditions under which individual jet flows, not fully mixed with the background turbulence, produce a spectral peak and the corresponding frequency associated with the jet forcing timescale.

List of symbols

$(u, v, w) = (u_1, u_2, u_3)$	Instantaneous velocities aligned with x, y, z coordinates
$\boldsymbol{e}_j$	Directional unit vector
ℓ_{DI}	Demarcation scale between inertial and dissipation ranges, estimated from the lower bound of the inertial subrange
ℓ_{EI}	Demarcation scale between energy-containing and inertial ranges, estimated from the upper bound of the inertial subrange
τ_F	Forcing timescale
η, u_η, τ_η	Kolmogorov microscales in length, velocity, and time
Γ	Gamma function
λ	Taylor microscale
$\langle\cdot\rangle$	Ensemble average
$\langle\epsilon\rangle$	Mean turbulent kinetic energy dissipation rate
$\mu_{\mathrm{on}}, \mu_{\mathrm{off}}$	Mean on/off time in sunbathing algorithm
ν	Kinematic viscosity
$\bar{\cdot}$	Spatial average over homogeneous region
ϕ	Source fraction in sunbathing algorithm
ρ_{ij}	Two-point autocorrelation
$\sigma_{\mathrm{on}}, \sigma_{\mathrm{off}}$	Standard deviation of on/off time in sunbathing algorithm
Ku	Kurtosis
Sk	Skewness
B	Jet centerline velocity-decay constant
D_J	Jet diameter
D_{ij}^2	Second-order structure function
$\mathrm{d}r$	Spatial resolution
f	Frequency
f_{exp}	Exponential fit to the autocorrelation function

✉ Nimish Pujara
npujara@wisc.edu

Joo Young Bang
jbang9@wisc.edu

[1] Department of Civil and Environmental Engineering, University of Wisconsin–Madison, Madison, WI 53706, USA

Published online: 06 November 2023

f_{model}	Model function fit to the autocorrelation function
$h(r)$	Osculating parabola fit to the autocorrelation function
J	Inter-jet spacing
k	Turbulent kinetic energy
K_q	Modified Bessel function of the second kind
L_A	Array-to-array distance
L_g	Grid spacing
L_{ij}	Integral length scale
L_{JM}	Jet merging distance
M_1	Mean flow-to-turbulence ratio
M_2	Kinetic energy of mean flow-to-turbulent kinetic energy ratio
P_{uu}	Power spectral density of u'
r	Spatial lag
Re_λ	Taylor scale Reynolds number
Re_J	Jet Reynolds number
Re_L	Turbulence Reynolds number
S	Jet half-width spreading rate
$t_{\text{on}}, t_{\text{off}}$	Duration of on/off signal
t_g	Grid thickness
t_A	Attachment thickness
$T_{I,w}$	Integral time scale estimated from the autocorrelation function up to the first zero-crossing
T_{wz}	Integral time scale in z direction using turbulent scales from w'
u'	Fluctuating velocity
u_{rms}	Root-mean-square velocity
U_C	Jet centerline velocity
U_J	Jet exit velocity
x, y, z	Laboratory coordinate
x_0	Virtual origin of jet
z_c	Vertical center of PIV field of view

1 Introduction

According to classical theories of turbulence, the statistical properties of turbulent motions whose size is small compared to the scale of energy injection are universal and locally homogeneous and isotropic (Frisch 1995; Pope 2000; Davidson 2015). This motivates much research into fundamental and applied aspects of turbulent flows using 'idealized turbulence' whose statistics are homogeneous and isotropic. For laboratory experiments, this has meant that the generation of idealized (homogeneous and isotropic) turbulent flow has been widely attempted in a variety of stirred tank configurations. Different configurations include flow driven by oscillating grids (e.g., Silva and Fernando 1994; Brunk et al. 1996; Blum et al. 2010; Poulain-Zarcos et al. 2022), impellers or rotating discs (e.g., Douady et al. 1991; Birouk et al. 1996; Voth et al. 1998; Moisy et al. 1999; Worth and Nickels 2011; Lawson and Dawson 2015; Dou et al. 2016; Bounoua et al. 2018; Pujara et al. 2021; Lawson and Ganapathisubramani 2021), loudspeakers (e.g., Hwang and Eaton 2004; Chang et al. 2012; Hoffman and Eaton 2021), jets (e.g., Variano and Cowen 2008; Goepfert et al. 2009; Carter et al. 2016; Johnson and Cowen 2018; Tan et al. 2023), amongst other methods (*e.g.,* Rensen et al. 2005).

The different configurations to stir fluid into a turbulent state can be divided into three useful categories: (1) whether the stirring is continuous and steady (e.g., oscillating grids, steady rotations of discs and impellers, continuous jets) or unsteady and randomized (e.g., randomly actuated jets and impellers); (2) whether the stirring is provided by a single unit from each direction (e.g., a pair of counter-rotating discs, a set of oscillating grids) or multiple units (e.g., an array of jets or impellers); and (3) whether the stirring is asymmetric (e.g., an oscillating grid or jet array on one side of the tank) or symmetric (e.g., jets, impellers, or loudspeakers acting from multiple sides of the tank). It is generally found that continuous forcing is able to achieve higher Reynolds number turbulence compared to randomized forcing, but at the cost of stronger mean flows, higher mean shear, and a smaller volume of homogeneous isotropic turbulence (Voth et al. 2002; Hwang and Eaton 2004; Variano et al. 2004; Blum et al. 2010; Roy and Acharya 2012; Pujara et al. 2021). Additionally, multi-unit forcing produces a complex flow compared to single-unit forcing, but potentially allows more control over the scales of motion (Variano and Cowen 2008; Pérez-Alvarado et al. 2016; Carter et al. 2016; Bounoua et al. 2018). Finally, while asymmetric forcing is unavoidable for certain setups (Variano and Cowen 2013; Johnson and Cowen 2020), symmetric forcing produces better homogeneity and isotropy over a larger region with a smaller mean flow (Zimmermann et al. 2010; Goepfert et al. 2009; Bellani and Variano 2013; Dou et al. 2016; Hoffman and Eaton 2021).

Here, we use flow data from a new facility where a column of water is stirred with four randomly actuated jet arrays arranged symmetrically around a vertical octagonal prism (see Fig. 1a) to gain a better understanding of how different aspects of multi-unit, unsteady and randomized stirring control the characteristics of turbulence produced. More specifically, we investigate how the turbulence statistics are influenced by the algorithm that controls the randomized stirring, the geometry of the jet arrangement, the size of the tank, and the properties of each jet. While such results have been previously reported from tanks with a single jet array (Variano and Cowen 2008; Pérez-Alvarado et al. 2016; Johnson and Cowen 2018) and two-facing jet arrays (Bellani and Variano 2013; Carter et al. 2016), we address some outstanding questions and extend this knowledge to a new tank geometry and study the influence of individual jets in more detail. Based on our

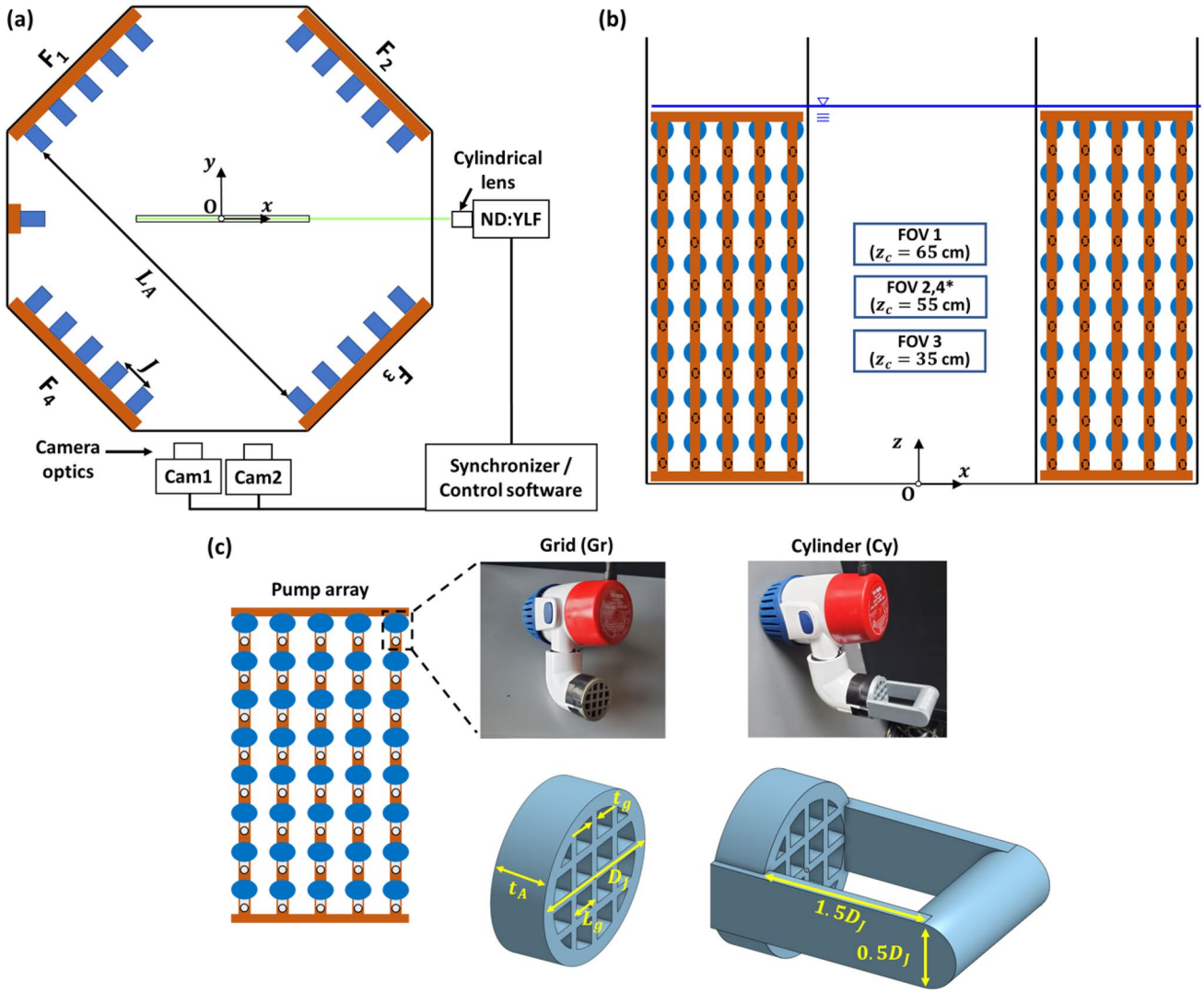

Fig. 1 Schematic diagram of experimental apparatus: (**a**) top view, (**b**) side view, and (**c**) pump arrays with the grid and cylinder attachments. There are four jet arrays, labeled F_1–F_4, placed on four vertical walls. The array-to-array distance is $L_A = 118$ cm, and the inter-jet spacing is $J = 12$ cm. A single pump located on the wall in the $-x$ direction is used only for the single pump experiments and is removed for the other experiments. Particle image velocimetry (PIV) data is taken at four fields of view (FOVs). The positions of FOVs1–3 are $x = \pm 16$ cm and $z = z_c \pm 5$ cm at $y = 0$. FOV4 is located at the same x and z position as FOV2, but in the $y = 7$ cm plane. The dimensions of the grid attachment are 2.66 cm nozzle exit diameter (D_J), 1.8 mm grid thickness (t_g), $\frac{1}{4}D_J$ grid spacing (L_g), and 1 cm thickness (t_A). The solidity (blockage) of the grid attachment is 41.8 %. The cylinder attachment has the same design as the grid attachment but has a horizontal cylinder of diameter $\frac{1}{2}D_J$ placed a distance $\frac{3}{2}D_J$ in front of the nozzle exit

data, we also provide recommendations on how to design such facilities and analyze turbulence data from them.

We begin in Sect. 2 with a review of the existing knowledge from previous facilities and point out some outstanding questions. Section 3 describes the details of the facility and measurements, with the flow analysis detailed in Sect. 4. We analyze the flow from a single jet in Sect. 4.1, which is followed by a systematic analysis of the turbulence in Sect. 4.2. In Sect. 4.3, we show the comparison between two and four jet arrays to specifically test the influence of additional jet arrays. A summary of the main results and implications for future research is given in Sect. 5.

2 Background

In this section, we review the existing knowledge from previous facilities to summarize current knowledge and highlight some of the outstanding questions.

Jet characteristics The flow characteristics of each forcing element are expected to affect the characteristics of turbulence in multi-unit forcing. For jets, the canonical non-swirling turbulent round jet is fully characterized by its Reynolds number $\mathrm{Re}_J = U_J D_J/\nu$, where U_J is the jet exit

velocity, D_J is the jet diameter, and ν is the kinematic viscosity of the fluid, and it is thought that once Re_J is high enough its value is less important than how the flow from different jets interact. However, since the flow from individual units is not typically characterized in detail, it is not clear whether manipulating the flow from each jet allows another way to control the turbulence produced.

Algorithm for randomized stirring The 'sunbathing' algorithm introduced by Variano and Cowen (2008) was found to randomize the jet firing pattern in time and space such that turbulent kinetic energy could be generated without produced a strong mean flow. An independent investigation (Pérez-Alvarado et al. 2016) confirmed the superiority of this algorithm over others, though it is notable that slightly different algorithms have been found to be most effective in active grids (Mydlarski and Warhaft 1998) and a tank stirred with vertical rotating paddles (Pujara et al. 2021). In the sunbathing algorithm, individual jets are turned on and off repeatedly, and the duration of each on/off period is chosen from Gaussian distributions described by $t_{\mathrm{on}} \sim N(\mu_{\mathrm{on}}, \sigma^2_{\mathrm{on}})$ and $t_{\mathrm{off}} \sim N(\mu_{\mathrm{off}}, \sigma^2_{\mathrm{off}})$, where μ_{on} and μ_{off} are the mean on/off times, and σ_{on} and σ_{off} are the standard deviations of the on/off times. Flow statistics were found to be insensitive to the standard deviations of the on/off times and the recommended values were based on the ratio $\sigma/\mu = 1/3$. With this ratio fixed, the only remaining free parameters are the mean on-time μ_{on} and the source fraction $\phi = \mu_{\mathrm{on}}/(\mu_{\mathrm{on}} + \mu_{\mathrm{off}})$, which represents the mean of the fraction of the pumps firing at any given time.

Investigations of the effects of the source fraction ϕ have found that its optimal value, where the root-mean-square velocities are maximized, is in the 5–25% range for a single array (Variano and Cowen 2008) and two-facing arrays (Lawson and Ganapathisubramani 2021). The low values of the optimal ϕ relate to the fact that turbulence production is maximized by the interaction of the flow from individual forcing units with the background flow. Turning on all units robs the flow from each unit to both contribute to and interact with an unsteady background.

The source fraction ϕ is a dimensionless quantity, but the mean on-time μ_{on} is generally reported as a dimensional quantity suggesting that the mechanism by which it influences the scales of turbulence is not fully understood. From systematic studies of varying μ_{on} (Variano and Cowen 2008; Carter et al. 2016; Pérez-Alvarado et al. 2016; Johnson and Cowen 2018), it is known that increasing μ_{on} increases the root-mean-square velocities and turbulence intensity until a certain value (different in each setup) at which point the effect saturates and further increases in μ_{on} do not produce further increases in the flow intensity. For impeller arrays, Lawson and Ganapathisubramani (2021) introduced a dimensionless mean on-time based on the impeller rotation frequency and found that this value needs to be high ($O(10^3)$). For jets, there are two natural choices for making the mean on-time dimensionless:

$$\frac{U_J \mu_{\mathrm{on}}}{D_J} \quad \text{or} \quad \frac{U_J \mu_{\mathrm{on}}}{\frac{1}{2} L_A}, \tag{1}$$

where L_A is a representative scale of the tank size. The first choice ($U_J \mu_{\mathrm{on}}/D_J$) is analogous to the jet's 'formation time' (Gharib et al. 1998) and postulates that the effects of mean on-time are related to flow development in an individual jet, while the second choice ($U_J \mu_{\mathrm{on}}/(\frac{1}{2} L_A)$) compares the distance traveled by the fluid during a typical on-cycle to the tank size, postulating that it is whether the flow from each jet 'reaches' the tank center that matters.

Homogeneity, isotropy, and scales of turbulence Homogeneity and isotropy are easier to achieve for symmetric forcing (Bellani and Variano 2013; Hwang and Eaton 2004, e.g., two-facing jet arrays or loudspeakers in all corners of a cube). While forcing from many different directions appears to be a common approach when using continuous forcing (Hwang and Eaton 2004; Hoffman and Eaton 2021; Bounoua et al. 2018), planar symmetry (two-facing arrays) is the most common configuration for randomized forcing (Bellani and Variano 2013; Carter et al. 2016; Lawson and Ganapathisubramani 2021). Two-facing arrays with randomized forcing commonly produce a relatively large region of homogeneous turbulence, but only Bellani and Variano (2013) seem to have achieved large-scale isotropy (measured by the ratio of root-mean-square velocities in the longitudinal and transverse directions with respect to the forcing). In Carter et al. (2016), the longitudinal (jet parallel) root-mean-square velocity is always higher than the transverse root-mean-square velocity, with 1.35 being the lower bound value for this ratio in their setup. Similarly, Esteban et al. (2019) find a root-mean-square isotropy ratio of 1.2. Bellani and Variano (2013) claim they achieve isotropy by optimizing the inter-array distance (L_A in our notation) and it has been previously noted that the centrifugal nature of the pumps may play a role, but we hypothesize that the jet arrangement in their setup is also important. The pumps driving the jets are connected to 90-degree elbows that are insufficiently long to ensure the jet axis is perpendicular to the array, but because each group of four pumps is rotated relative to each other in the array plane, the net effect is flow isotropy in the tank center. The other notable results from previous studies are that doubling the inter-jet spacing J has little effect on the turbulence statistics and placing a mesh grid in front of

each array reduces the turbulence intensity and integral scale in the tank center (Carter et al. 2016).

Interestingly, Lawson and Ganapathisubramani (2021) are able to produce homogeneous turbulence in a volume that is a significant fraction of the tank volume, and though their root-mean-square velocity isotropy ratio is of a similar magnitude to other facilities, it is the longitudinal velocity component that is weaker. Both of these effects appear to be related to the fact that, with impellers driven randomly in both directions, the forcing algorithm drives momentum towards the tank center as well as back towards tank walls. This significantly reduces the merging distance and pumps more energy into the transverse component of velocity.

Apart from homogeneity and isotropy, it would be desirable to be able to predict the scales of turbulence based on a given tank design: the root-mean-square velocity (i.e., turbulent kinetic energy), the integral scale of turbulence, and the turbulent kinetic energy dissipation rate. As discussed above, previous results show that these quantities increase with mean on-time μ_{on} (up to a saturation point) and vary non-monotonically with the source fraction ϕ (with a peak in the range 5–25%), but it is not clear what sets the scales of turbulence in the first place and why there is a saturation point for them with increasing mean on-time.

Jet merging For a jet-stirred tank, the idea of jet merging is that the discharge of each jet should lose its distinctive characteristics by merging with the background turbulence over a certain distance known as the jet merging region.

For continuously operating jets, scaling arguments from canonical turbulent round jets can be used to predict the distance over which adjacent jets merge: The jets will merge when their half-widths intersect:

$$2SL_{JM} = J \tag{2}$$

Here, L_{JM} is the jet merging distance, J is the inter-jet spacing, and S is the jet half-width spreading rate. Using $S \approx 0.09$ (Pope 2000) gives $L_{JM} \approx 5.5J$; for experimental evidence for this value, see Tan et al. (2023). In jet arrays with unsteady and randomized forcing, two main factors can be expected to cause deviation of L_{JM} from this value. First, the background (turbulent) flow affects the spreading rate S; it is found that jets in a turbulent environment are wider, their width grows faster compared to a quiescent background, their axial velocities are arrested when the local background turbulence velocity is of the same order as the axial velocity, and their structures are broken when the background turbulence and jet root-mean-square velocities are approximately equal (Guo et al. 2005; Khorsandi et al. 2013; Sahebjam et al. 2022). Second, since not all jets are always on, the effective inter-jet spacing is a function of the source fraction; this effective inter-jet spacing will be larger than J though it is still expected to scale with J. While the first fact decreases the jet merging distance, the second fact increases it.

Evidence from a single randomly actuated jet array (Variano and Cowen 2008; Pérez-Alvarado et al. 2016; Johnson and Cowen 2018) suggests that these two effects may roughly cancel each other out. It was found that the signature of individual jets could not be observed on the free surface above a depth of $6J$ for an upwards-pointing jet array placed at the bottom of a water tank. Similarly, profiles of root-mean-square velocities become uniform in directions parallel and perpendicular to the jet array at a distance of approximately $6J$ (before starting to decay as distance from the jet array increases further). For two jet arrays on opposite sides of the tank that face each other (Bellani and Variano 2013; Carter et al. 2016), the data again support that $L_{JM} \approx 6J$ is reasonable; the flow statistics become homogeneous at this distance from each jet array.

While the jet merging distance in these previous studies is taken to be the distance from the jet array until the point where turbulence statistics become homogeneous, this does not factor in the degree to which individual jet flows are discernible in instantaneous measurements. If jet flows are not fully merged with the background turbulence by this metric, their characteristics are likely to be detected in the turbulent velocity power spectra at the appropriate forcing timescale. Based on the unsteady nature of the forcing in the sunbathing algorithm, several candidates have been proposed for this forcing timescale (Variano and Cowen 2008; Lawson and Ganapathisubramani 2021):

$$\tau_{F1} = \mu_{on} + \mu_{off} = \frac{\mu_{on}}{\phi}; \quad \tau_{F2} = \mu_{on}; \quad \tau_{F3} = \phi\mu_{on}, \tag{3}$$

where we have used the relation $\phi = \mu_{on}/(\mu_{on} + \mu_{off})$ in the definition of τ_{F1}. These candidate forcing timescales all increase with μ_{on}, but differ in the role of ϕ.

3 Experiments

3.1 Turbulence tank

The tank shown is an octagonal cylinder shape with a side of 61 cm and a height of 122 cm, constructed with acrylic plates supported by an aluminum frame (Fig. 1). We place our coordinate system origin at the center of the tank bottom with the coordinates x and y comprising the horizontal plane and z pointing in the vertical direction against gravity. During operation, the tank is filled with water (via a 20-micron filter) up to a depth of 100 cm and kept in a temperature-controlled room such that the water temperature is 25.4 C with kinematic viscosity $\nu = 8.85 \times 10^{-7}$ m^2

/s. Turbulence is generated by fluid forcing from four arrays of pumps on the vertical walls arranged so that there are two sets of orthogonal facing arrays. The distance between facing arrays is $L_A = 118$ cm, which also accounts for the attachments on each pump described below. Each array has 8 rows of 5 pumps (Rule 360 GPH bilge pump), and the spacing between adjacent pumps is $J = 12$ cm. The bottom row and two side columns are $J/2 = 6$ cm away from the wall ends, but the top row is 10 cm away from the water surface to ensure the base of the pumps is fully submerged. This configuration with mirror symmetry with the walls is known to minimize secondary flow in oscillating grid tanks (Fernando and De Silva 1993).

Each pump creates a synthetic jet by drawing water radially from its base and injecting it from the outlet. We connected 90-degree elbows so that the outlet directs the flow towards the tank center with a jet exit diameter of $D_J = 2.66$ cm. In preliminary experiments, we found that the elbow does not fully bend the flow and the jet exit velocity was not normal to the outlet face. It is also well known that bends generate secondary swirling flows. Thus, to straighten and condition the flow, we attach a 3D-printed grid to the outlet of each pump (Fig. 1c).

When operated together, the pumps are controlled by solid-state relays (SSR-Rack48, Measurement Computing Corporation) which can open and close the circuit to 12 V power supplies. The circuits also have power distribution boards with 5 A fuses to protect the circuit and pumps. Two 96-channel digital input/output modules (PCIe-6509, National Instruments) are connected to the racks to trigger the relay modules. With this configuration, we can control individual pumps using custom MATLAB (MathWorks) code. To drive the pumps, we adopt the sunbathing algorithm (Variano and Cowen 2008) described in Sect. 2.

3.2 Flow data collection

Random-jet-stirred turbulence (particle image velocimetry data) We conduct velocity measurements using particle image velocimetry (PIV) under a range of different parameters for the sunbathing algorithm that controls the jets with a fixed tank geometry. We test two source fractions: Low ($\phi = 6.25\%$) and High ($\phi = 12.5\%$). While $\phi = 12.5\%$ was found to be the optimal value for a single jet array (Variano and Cowen 2008), we also test a lower value to check whether this lower value gives better performance than the previously found optimal value with the increased number of jet arrays in our setup. We also test three different mean on-times: $\mu_{on} = [1.5, 3, 6]$ s to understand the growth and saturation of turbulence intensity as a function of the mean on-time. Finally, we test the effect of attachments at the pump outlets to understand how manipulations of individual forcing elements affect the scales of turbulence. The pumps with grid attachments are considered the baseline case and the pumps with a grid and a horizontal cylinder attachment are the new test case (Fig. 1c). We hypothesized that including a horizontal cylinder would weaken the jet and increase vertical stirring via flow separation around the cylinder, both of which should contribute to improved homogeneity and isotropy of the turbulence. In all, there are 12 different experimental conditions, as summarized in table 1.

Velocity fields are measured with 2D planar PIV (Fig. 1): A 527 nm Nd-YLF laser (Photonics Industries) with a cylindrical lens located at $+x$ side wall creates a light sheet with an average thickness of 1.5 mm in the x-z plane. Images are taken with cameras (Phantom VEO340; 2560 px × 1600 px with 10 μm px size) installed at $-y$ side wall. Each camera is mounted with a 100 mm lens (Tokina) and fitted with a 527 nm bandpass filter. The flow is seeded with tracer particles (10 μm median diameter hollow microspheres with a specific gravity of 1.10 ± 0.05; Potter Industries 110P8).

Table 1 PIV experimental conditions

Case	Attachment	ϕ (%)	μ_{on} (s)	μ_{off} (s)	σ_{on} (s)	σ_{off} (s)
GrLo15	Grid	6.25	1.5	22.5	0.5	7.5
GrLo30		6.25	3.0	45.0	1.0	15.0
GrLo60		6.25	6.0	90.0	2.0	30.0
GrHi15		12.5	1.5	10.5	0.5	3.5
GrHi30		12.5	3.0	21.0	1.0	7.0
GrHi60		12.5	6.0	42.0	2.0	14.0
CyLo15	Cylinder	6.25	1.5	22.5	0.5	7.5
CyLo30		6.25	3.0	45.0	1.0	15.0
CyLo60		6.25	6.0	90.0	2.0	30.0
CyHi15		12.5	1.5	10.5	0.5	3.5
CyHi30		12.5	3.0	21.0	1.0	7.0
CyHi60		12.5	6.0	42.0	2.0	14.0

To examine the homogeneity of the turbulent flow in the vertical extent, we took velocity data at three different field of views (FOVs) (Fig. 1b). Using two cameras side-by-side, we captured velocity data covering $x = \pm$ 16 cm and $z = z_c \pm 5$ cm, where z_c is the vertical center of each FOV, at $y = 0$. To check that the flow was homogeneous away from the center plane, we also took data at FOV4, which was located at the same x-z coordinates, but at $y = 7$ cm. The magnification factor in these images is approximately 14 px/mm, and the time interval between image pairs is adjusted to give a maximum particle displacement of 5–7 pixels. At each FOV, we took 1460 image pairs with a 0.5 Hz sampling rate.

Image processing to obtain velocity fields is conducted using DaVis v10 (LaVision). Since particle intensities can vary significantly across the FOV, we use a nonlinear filter to match the dynamic range of the particle intensities within each image (Adrian and Westerweel 2011), which significantly improves the signal-to-noise ratio. Velocity vectors are calculated using an iterative cross-correlation method with four passes for each image pair. The first 64×64 px pass is followed by three passes at 32×32 px with 75 % overlap. The spatial resolution is about 3 to 5 times the Kolmogorov length scale, which in turn, is sufficient to capture more than 95% of the turbulent kinetic energy (Saarenrinne et al. 2001). Sub-pixel accuracy in the pixel displacement in each sub-window is achieved using a Gaussian fitting function to the correlation maximum and neighboring pixels. Each velocity vector is quality-checked by comparing the relative heights of the first and second peaks in the correlation field. We achieve more than 95% valid vectors and low-quality vectors are removed (without interpolation) from the analysis.

Random-jet-stirred turbulence (acoustic Doppler velocimetry data) We also perform single-point measurements using an acoustic Doppler velocimetry (ADV, Nortek Vectrino). While the PIV measurements allow us to understand the spatial variation of turbulence under a range of different forcing conditions with a fixed tank geometry, we use the ADV measurements to understand the effect of changing the tank geometry. In one set of tests, we systematically vary the mean on-time and the array-to-array distance to understand their combined effects on the turbulence at the tank center while keeping a constant source fraction $\phi = 12.5\%$. In this case, we test five different mean on-times ($\mu_{\text{on}} = [0.8, 1.5, 3.0, 4.5, 6.0]$ s) with $\frac{1}{2}L_A = 59.0$ cm and another five different mean on-times ($\mu_{\text{on}} = [0.7, 1.3, 2.5, 3.7, 5.0]$ s) with $\frac{1}{2}L_A = 48.5$ cm. These tests are designed to have comparable values of the dimensionless mean on-time $U_J\mu_{\text{on}}/(\frac{1}{2}L_A)$ for different array-to-array distances. In another set of tests, we turn off all pumps in arrays of F_2 and F_4 (Fig. 1a) to obtain data that compares turbulence produced by two arrays to turbulence produced by all four arrays. In this case, since we only focus on the effect of the array geometry, we fix $\phi = 12.5\%$ and vary $\mu_{\text{on}} = [1.5, 3, 6]$ s.

All ADV measurements are taken at the tank center at $z = 54$ cm, which corresponds to the centerline of a row of jets. The coordinate system of the ADV measurements is such that one-pair of the ADV beams is aligned with the forcing directions from the pumps in arrays F_1 and F_3. Velocity data are recorded at a sampling rate of 50 Hz with a sampling volume and transmit length of 7 mm and 1.8 mm, respectively. To ensure the statistical convergence of turbulent scales, we record data in each case for more than 30 min.

Single jet flow (particle image velocimetry data) To complement velocity measurements of turbulence driven by randomly actuated jets, we also conduct experiments where the flow due to a single pump is measured in a time-resolved manner with an otherwise quiescent background. A single pump is positioned at the $-x$ side wall at $z = 50$ cm (Fig. 1a) so that the light sheet bisects the pump's outlet. PIV measurements are taken at the tank center using one camera with a FOV that covers $x = \pm 7$ cm and $45 \leq z \leq 55$ cm. This setup allows for data of the pump jet's far-field velocity to be obtained. To obtain velocity data in the near-field, we move the pump along the x-axis, while keeping the FOV the same. We take data of the pump with the grid attachment and with the cylinder attachment with the cylinder axis parallel to the y-axis. We measure the jet's velocity profile in continuous mode and in a single pulse mode with pulse durations of 1.5, 3, and 6 s to mirror the mean on-times used to generate turbulence.

4 Flow analysis

4.1 Velocity from a single jet

We begin with analysis of the statistically steady jet produced by a single pump operated in continuous mode with the grid and cylinder attachments. The velocity data are decomposed into a temporal mean and fluctuating component, with root-mean-square velocities calculated from the fluctuating component. The profiles of the mean and fluctuating components are shown in Fig. 2. We find that the grid attachment successfully conditions the flow so that the resulting jet resembles a canonical non-swirling round jet with flow normal to the outlet. The cylinder attachment creates a wake at the jet centerline in the near-field (Fig. 2a), and while this velocity deficit is smoothed out into a weaker and broader jet relative to the grid attachment by the time the jet reaches the tank center (Fig. 2b),

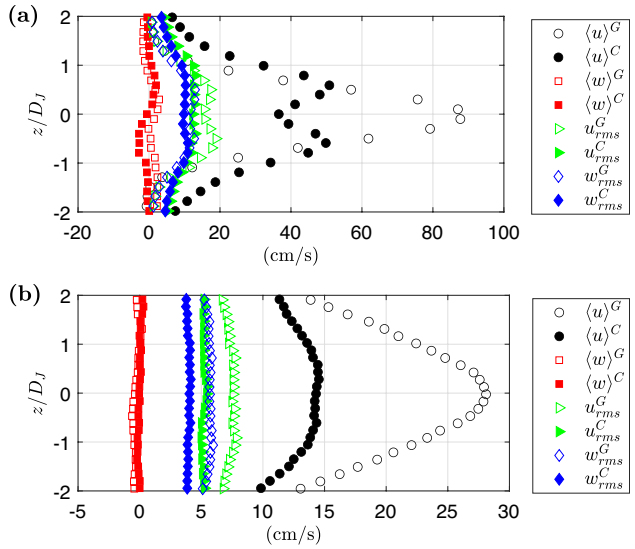

Fig. 2 Velocity profiles of continuous jet flow with the grid attachment and cylinder attachment in the near field $x = 5D_J$ (**a**) and at the tank center $x = \frac{1}{2}L_A$ (**b**). The superscripts refer to the grid (G) and cylinder (C) attachments, respectively

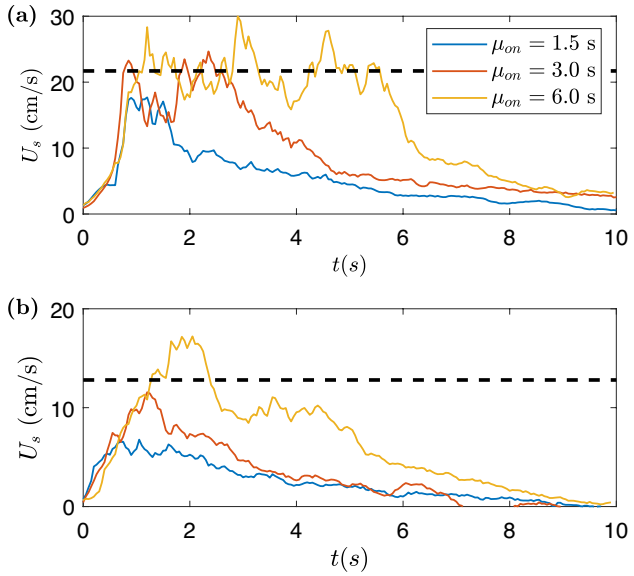

Fig. 3 Temporal evolution of the spatially averaged axial velocity (U_s) with the pulse firing with the grid (**a**) and cylinder (**b**) attachments. Dashed lines represent U_s from continuous jet flow experiments. This figure shows representative data, but we observed a consistent trend across all repetitions

the flow does not recover to a canonical turbulent round jet. In particular, the radial profiles of the mean axial velocity and the normalized Reynold stresses exhibit that the flow has a higher jet half-width spreading rate and stronger turbulent intensity compared to those from the canonical turbulent round jet in the self-similar region.

In order to better understand random-jet-stirred turbulence data below, we also estimate the jet exit velocity U_J from the continuous jet data. We do so by applying the known centerline velocity decay for canonical turbulent round jets

$$\frac{U_C(x)}{U_J} = \frac{\mathrm{BD}_J}{(x - x_0)}, \tag{4}$$

where U_C is the centerline velocity, $B = 6.06$ is the jet centerline velocity-decay constant, and x_0 is the virtual origin (Pope 2000). We find $U_J = 82.2$ cm/s with $x_0 = 2.70D_J$ for the grid attachment. While the flow from the cylinder attachment does not strictly follow the relationships found in canonical turbulent round jets, applying Eq. (4) nonetheless provides a reasonable estimate. We find $U_J = 49.6$ cm/s with $x_0 = 1.21D_J$ for the cylinder attachment, which is within 5% of the value found from estimating the jet exit velocity using the peak axial velocities in the near-field velocity data (Fig. 2a).

We next consider the velocity data from the single jet operated in a single pulse into an otherwise quiescent background, where the pulse lengths are 1.5 s, 3 s, or 6 s (to mirror the mean on-times used in the sunbathing algorithm to produce random-jet-stirred turbulence). To compare the time evolution of the axial velocity field across different on-times, we calculate the velocity U_s, which is the axial velocity averaged over $z/D_J = \pm 2$ at the tank center. The results in Fig. 3 show that the velocity magnitude in pulsed mode is smaller than in continuous mode for pulse lengths of 1.5 s and 3 s. For a pulse length of 6 s, we see that the axial velocity is essentially the same as that in a continuous jet.

The reduced axial velocity compared to a continuous jet for short pulse lengths is related to: (1) formation of a vortex ring during the jet start-up due to a spiral roll-up flow separation at the nozzle (Gharib et al. 1998); and (2) diffusion of axial momentum as the pulsed jet flow travels to the tank center. We note that the pump ramp-up time is short compared to our pulse lengths, so it is not expected to play a significant role. For the starting vortex, it is known that such a vortex ring absorbs the momentum of the discharged fluid and grows in size even after it detaches from the nozzle by absorbing momentum from the trailing jet (Schram and Riethmuller 2001; Gao and Yu 2010). However, for a large jet formation time ($U_J \mu_{\mathrm{on}}/D_J \gg 4$, Gharib et al. 1998), which is the case for all pulse lengths tested here, the energy absorption by the starting vortex ring is marginal. Thus, the most important effect must be the diffusion of axial momentum, which is a function of how far the fluid must travel ($\frac{1}{2}L_A$ in this case).

4.2 Random-jet-stirred turbulence

Figure 4 shows instantaneous snapshots of the velocity field at FOV2 for the GrLo30 case. The flow fields, which

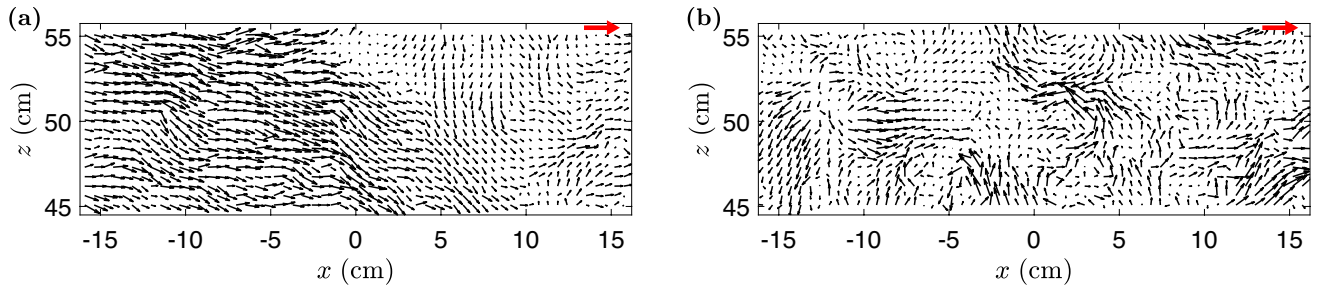

Fig. 4 Instantaneous velocity snapshots at FOV2 of the GrLo30 case corresponding to the maximum (**a**) and minimum (**b**) instantaneous kinetic energy. For visual clearance, only every 10th vector is shown. The red arrows show a magnitude of 40 cm and 10 cm/s, respectively, for reference

correspond to snapshots with the maximum and minimum instantaneous kinetic energy, exhibit rotation and shear at various scales that are the hallmarks of turbulent flow.

To conduct further analysis, we subject the velocity data to a Reynolds decomposition where the instantaneous velocity field $\boldsymbol{u} = (u, v, w) = (u_1, u_2, u_3)$, which is aligned with (x, y, z) coordinates, is decomposed into an ensemble-averaged velocity $\langle \boldsymbol{u} \rangle$ and fluctuating velocity $\boldsymbol{u}'$

$$\boldsymbol{u}(\boldsymbol{x}, t) = \langle \boldsymbol{u} \rangle + \boldsymbol{u}', \tag{5}$$

where the ensemble average $\langle \cdot \rangle$ is computed over all velocity snapshots. From the fluctuating velocity field, we compute root-mean-square (RMS) of the fluctuations in a given component $u_{\text{rms}} = [\langle u'^2 \rangle]^{1/2}$ and the turbulent kinetic energy (TKE) $k = (\langle u'^2 \rangle + \langle v'^2 \rangle + \langle w'^2 \rangle)/2 \approx (2\langle u'^2 \rangle + \langle w'^2 \rangle)/2$. The approximation in computing k comes from assuming horizontal isotropy. Since we force the flow from four orthogonal horizontal directions, we expect that flow statistics are invariant to rotations about the z axis (i.e., $u_{\text{rms}} = v_{\text{rms}}$). In the subsequent analysis, we also use a spatial average $\bar{\cdot}$, which is computed over space in each FOV in the central region of the tank, $|x| < 10$ cm. Within this region, the statistics of turbulence are homogeneous, as shown in Sect. 4.2.1.

The normalized probability density functions (PDF) of the fluctuating velocities in the homogeneous region at FOV2 for the GrLo30 case are displayed in Fig. 5 with Gaussian distributions of zero mean and standard deviation of 1. The moments of $\boldsymbol{u}'$ in the homogeneous region at FOV2 are also summarized in Table 2. The skewness (Sk) is negligible, but the kurtosis (Ku) is greater than 3 indicating that extreme values in the fluctuating velocities are more likely than in a Gaussian distribution, which can also be seen in the tails of the PDFs in Fig. 5b. We expect that tails of these distributions are affected by the jet stirring (Veeravalli and Warhaft 1989; Yamamoto et al. 2022).

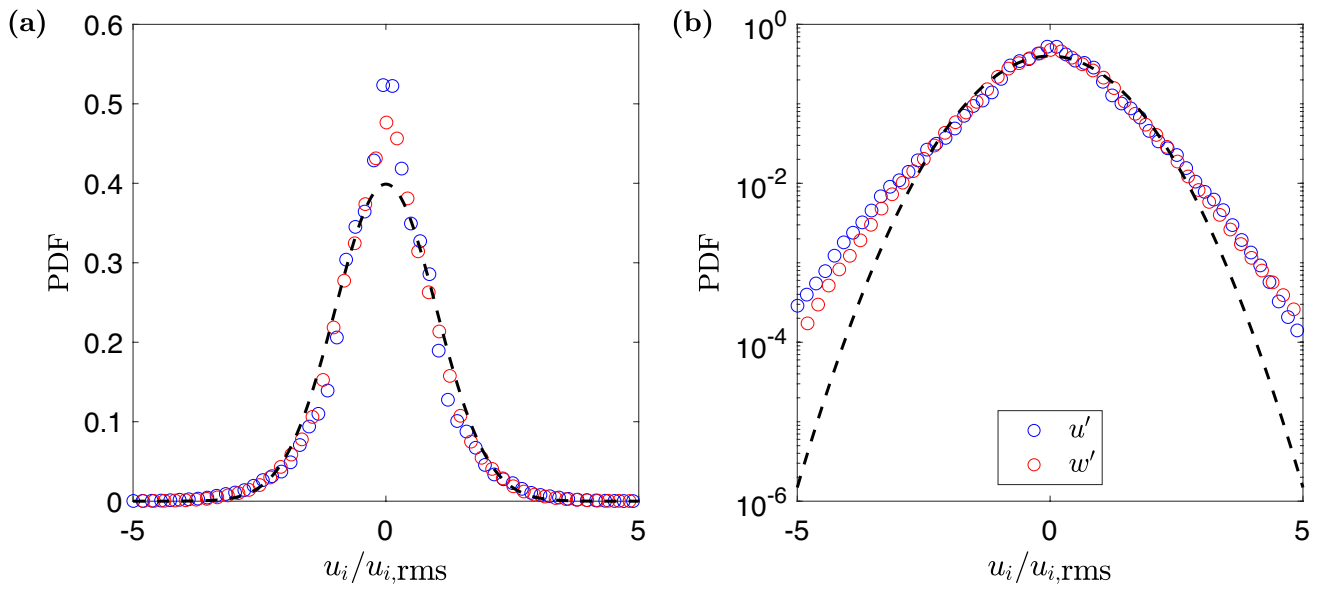

Fig. 5 The normalized PDFs of fluctuating velocity at FOV2 of GrLo30 case plotted in linear (**a**) and log (**b**) scales. The dashed lines indicate Gaussian distributions with zero mean and standard deviation of 1

Table 2 One-point turbulence statistics in the homogeneous region at FOV2

Case #	$\overline{\langle u \rangle}$ (cm/s)	$\overline{\langle w \rangle}$ (cm/s)	$\overline{u_{\mathrm{rms}}}$ (cm/s)	$\overline{w_{\mathrm{rms}}}$ (cm/s)	Sk(u')	Sk(w')	Ku(u')	Ku(w')	$\overline{u_{\mathrm{rms}}/w_{\mathrm{rms}}}$	M_1	M_2
GrLo15	−0.31	−0.21	5.8	4.5	−0.03	−0.07	4.38	4.01	1.3	0.052	0.004
GrLo30	−0.26	−0.42	6.7	5.0	−0.11	−0.02	4.52	4.06	1.3	0.052	0.003
GrLo60	−0.13	−0.44	7.1	5.0	−0.05	−0.04	4.50	4.26	1.4	0.038	0.002
GrHi15	−0.71	0.16	5.9	4.8	−0.13	−0.03	4.06	3.62	1.3	0.097	0.014
GrHi30	−0.38	−0.07	7.5	5.9	−0.08	−0.03	3.72	3.47	1.3	0.046	0.003
GrHi60	−0.64	−0.30	8.4	6.4	0.01	−0.03	3.57	3.38	1.3	0.069	0.006
CyLo15	−0.21	−0.52	3.7	2.9	−0.17	−0.17	4.43	3.88	1.2	0.097	0.013
CyLo30	0.09	−1.2	4.7	3.6	0.05	−0.17	4.12	3.70	1.3	0.12	0.029
CyLo60	−0.10	−1.16	5.2	3.8	−0.07	−0.26	4.08	3.71	1.4	0.11	0.022
CyHi15	−0.56	0.51	3.6	3.0	−0.12	−0.11	4.23	3.61	1.2	0.16	0.031
CyHi30	−0.06	−0.79	4.8	3.9	−0.07	−0.08	3.81	3.34	1.2	0.093	0.013
CyHi60	−0.32	−1.2	5.7	4.4	−0.03	−0.03	3.57	3.32	1.3	0.12	0.020

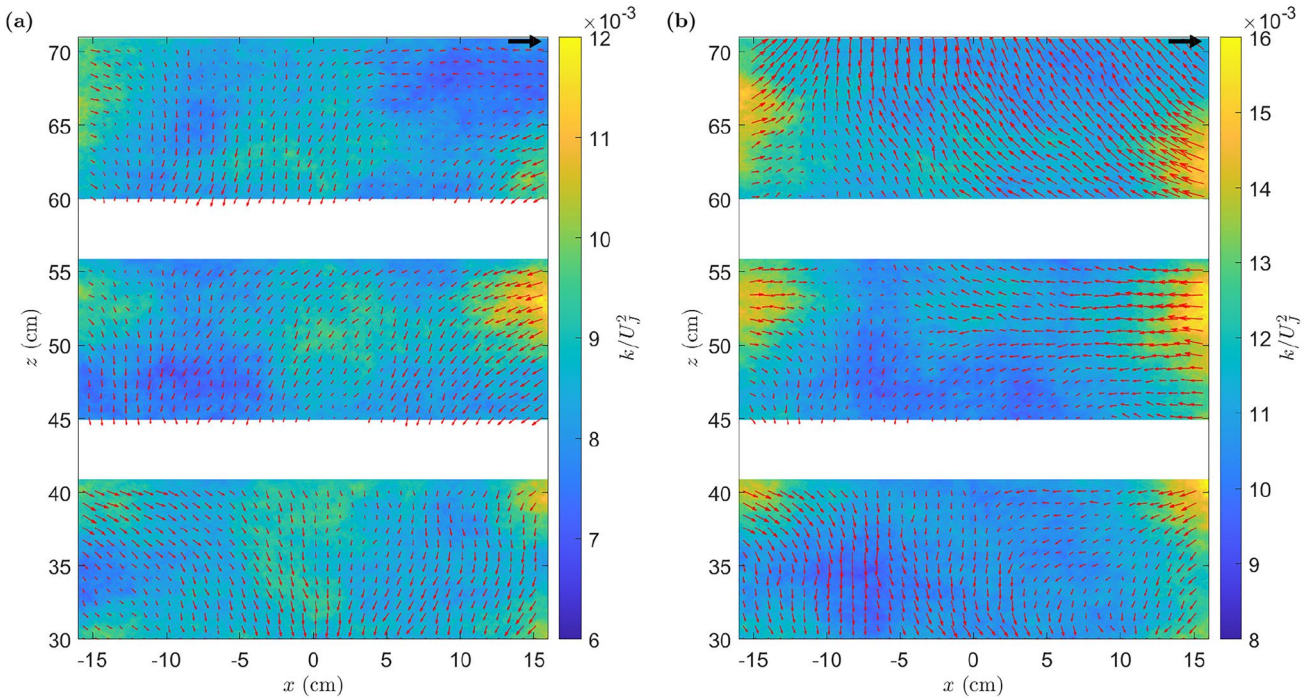

Fig. 6 Ensemble averaged velocity and TKE fields for GrLo30 (**a**) and GrHi30 (**b**) over FOVs1–3 ($y = 0$ plane). The large black arrows show a magnitude of 2 cm/s. The color axes for the dimensionless TKE span a factor of 2 between the minimum and maximum values

4.2.1 The homogeneous turbulence region and statistical jet merging

Figure 6 presents the ensemble-averaged velocity and the normalized TKE fields for FOVs1–3 for the GrLo30 and GrHi30 cases. Examining the TKE fields, we note that it is relatively homogeneous in the $|x| < 10$ cm region within each FOV. Specifically, the standard deviation of TKE in space is less than 5% of its spatial mean $\overline{k}$, and moreover, $\overline{k}$ has very similar values across FOVs. Additionally, for $|x| > 10$ cm, we see local patches of increased TKE at $z \approx 42$, 54, and 66 cm, which are the heights of the jets, but these 'statistical jet signatures' are absent for $|x| < 10$ cm. This is true for both the low and high source fraction data shown in the figure.

Defining the 'statistical jet merging distance' L_{JM} as the distance from the jet array to the point where turbulent statistics are homogeneous, the data show that the value is not sensitive to the parameters of the sunbathing algorithm (ϕ and μ_{on}) or the presence of jet exit attachments lending

support to the idea that $L_{JM} \sim J$ (Eq. (2)). However, we observe homogeneous statistics at a shorter distance ($L_{JM} \approx 4J$) than the previously accepted value ($L_{JM} \approx 6J$). We attribute this shorter jet merging distance to the presence of the additional arrays. While jet flows from single or two-facing arrays first mix with adjacent jets from the same array, the presence of jet arrays oriented perpendicular to each other in our setup allows mixing of jets across arrays, resulting in shorter statistical jet merging distances.

4.2.2 Large-scale isotropy and mean shear

The geometry of the tank setup ensures that flow statistics are isotropic in the horizontal directions. To investigate large-scale isotropy of the flow in the vertical *vs.* horizontal directions, Fig. 7 shows the spatially averaged ratio of the RMS velocities, which should be unity for large-scale isotropy. We observe values in the range 1.21–1.44 for the grid attachment and 1.1–1.39 for the cylinder attachment. Higher source fraction ϕ and smaller mean on-time μ_{on} give better performance in terms of achieving large-scale isotropy, consistent with previous results (Variano and Cowen 2008; Pérez-Alvarado et al. 2016; Carter et al. 2016; Johnson and Cowen 2018). These trends can be understood by considering how an individual jet interacts with the existing background turbulence when it is fired into. While flow from each jet has the majority of its momentum in the jet-axial direction, the background turbulence that the jet travels into serves to break up the jet structure. For larger μ_{on}, a larger patch of fluid that retains the anisotropic signature of the jet flow is set into motion, whereas for larger ϕ, this patch must contend with a higher intensity background flow which breaks it up more effectively resulting in more isotropic statistics.

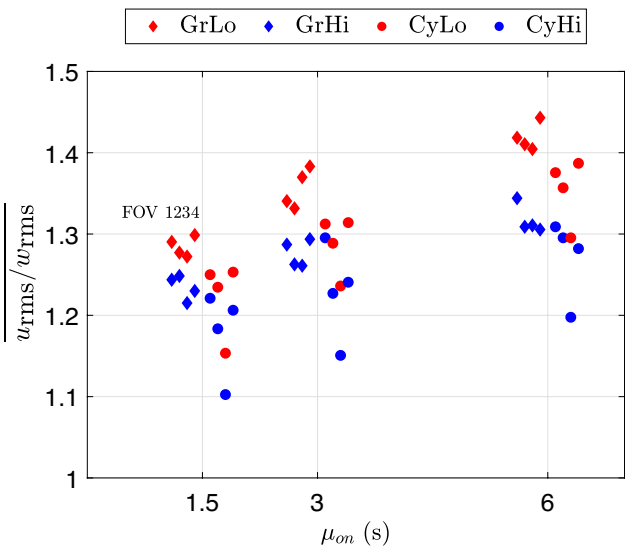

Fig. 7 Spatially averaged RMS velocity ratio as a function of μ_{on}, shown on the x-axis (1.5, 3, and 6 s), for the grid attachment (diamond) and the cylinder attachment (circles), which are respectively represented on the left and right sides of the corresponding μ_{on}. The source fraction is illustrated by different colors, red ($\phi = 6.25\%$) and blue ($\phi = 12.5\%$). Data for FOVs1–4 for the same mean on-time are displayed by offsetting them with respect to each other (left to right), as shown by the text

The cylindrical attachment results in only a slight improvement in the large-scale isotropy, despite the weakened and wider velocity profiles observed in the single jet data (Fig. 2). The reason is that while there is clear evidence of flow separation and more vertical mixing in the jet's near field, the far-field statistics such as $\langle u \rangle / w_{rms}$ or u_{rms}/w_{rms} are found to be similar to the grid attachment. It appears that since jets with manipulated exit conditions still relax to have properties analogous to canonical jets in the far field, the improvements in isotropy are small.

Another metric of large-scale isotropy is Reynolds stress tensor, where the off-diagonals are zero for isotropic turbulence. In other words, u' and w' should be uncorrelated and no mean shear should exist. To evaluate the correlation between u' and w', the normalized Reynolds stress (NRS) is calculated by

$$\mathrm{NRS} = \overline{\left(\frac{|\langle u'w' \rangle|}{u_{rms} w_{rms}} \right)} \tag{6}$$

The absolute value is applied prior to spatial averaging in order to prevent the Reynolds stress in certain regions from being canceled out by other regions due to different signs. The normalized Reynolds stress is less than 5 % for the grid and 7 % for the cylinder cases, suggesting that there is negligible correlation between velocity fluctuations and hence negligible TKE production in the tank center.

4.2.3 Mean flow structure and magnitude

Examples of the mean flow field ($\langle u \rangle$, $\langle w \rangle$) are shown in Fig. 6. While the mean flow is always small compared to the fluctuating flow field, we find that its structure depends on the parameters of the sunbathing algorithm. The $\langle u \rangle$ fields generally show inward-directed flows due to how the jets are directed, but the $\langle w \rangle$ fields change sign depending on the parameters of the sunbathing algorithm. For example, in the grid attachment cases, $\overline{\langle w \rangle}$ is positive (upward directed) at FOV1, whereas $\overline{\langle w \rangle}$ is negative (downward directed) with the cylinder attachment at $\mu_{on} = 3$ and 6 s at FOVs2–3. From continuity considerations, the jet flows directed horizontally towards the tank center must recirculate back towards the arrays. One would expect this recirculation to occur at the top and bottom of the tank where there are no arrays with a preference for the top of the tank where there is reduced friction due to the free surface. This would suggest upward directed mean flow in the tank center,

but at times we also observe downward directed mean flow and preferential return via the bottom of the tank. One possible explanation for this is the small amount of heat generated by the submerged pumps that could induce flow upwards adjacent to the pumps, which then sets a mean flow structure with downward vertical velocities. This mechanism is likely to be important in all tanks where the flow driving mechanism (e.g., pump, motors) is not thermally isolated from the working fluid.

To demonstrate that the mean flow is weak compared to the turbulence in the homogeneous region, we use the metrics

$$M_1 = \overline{\left(\frac{2|\langle u \rangle| + |\langle w \rangle|}{2u_{\mathrm{rms}} + w_{\mathrm{rms}}} \right)} \tag{7a}$$

$$M_2 = \overline{\left(\frac{2\langle u \rangle^2 + \langle w \rangle^2}{2u_{\mathrm{rms}}^2 + w_{\mathrm{rms}}^2} \right)}. \tag{7b}$$

M_1 compares the magnitude of the mean flow to the turbulence RMS velocity, and the absolute value of the mean velocity is used to avoid excessive minimization of M_1 by the spatial averaging. M_2 represents the ratio of the kinetic energy of the mean flow to the turbulence. Using the cut-off value of $M_1 < 0.1$, we find four cases (GrLo15, 30, 60, and GrHi30) that satisfy this criterion for all FOVs. For these cases, $M_2 < 0.01$ (i.e., the TKE is more than 100 times larger than the kinetic energy of the mean flow). Surprisingly, all cases with the cylindrical attachment have $M_1 > 0.1$. A closer examination reveals that mean flows for both attachments have relatively similar magnitudes, but the cases with the cylindrical attachment have smaller values of $\boldsymbol{u}_{\mathrm{rms}}$ leading to higher values of M_1 and M_2.

M_1 and M_2 are always less than 0.2 and 0.05, respectively, showing the mean flow is weak compared to the turbulence fluctuations. Overall, the mean flow magnitude is not a function of the jet attachments and the parameters of the sunbathing algorithm, but its structure is.

4.2.4 Scales of motion: RMS velocities

Figure 8 summarizes the values of the mean and RMS velocities at all FOVs across all experimental conditions. Apart from providing further evidence of low mean flows and flow homogeneity ($\overline{u_{\mathrm{rms}}}$ and $\overline{w_{\mathrm{rms}}}$ are near identical at all FOVs and their spatial variations are small compared to their spatial means), the data also show that RMS velocities are functions of the parameters of the sunbathing algorithm (μ_{on} and ϕ) and of the attachments at the jet exit. Larger ϕ and μ_{on} generate turbulent flow with larger RMS velocities, as previously found (Variano and Cowen 2008; Carter et al. 2016), and the cylindrical attachment weakens the RMS velocities.

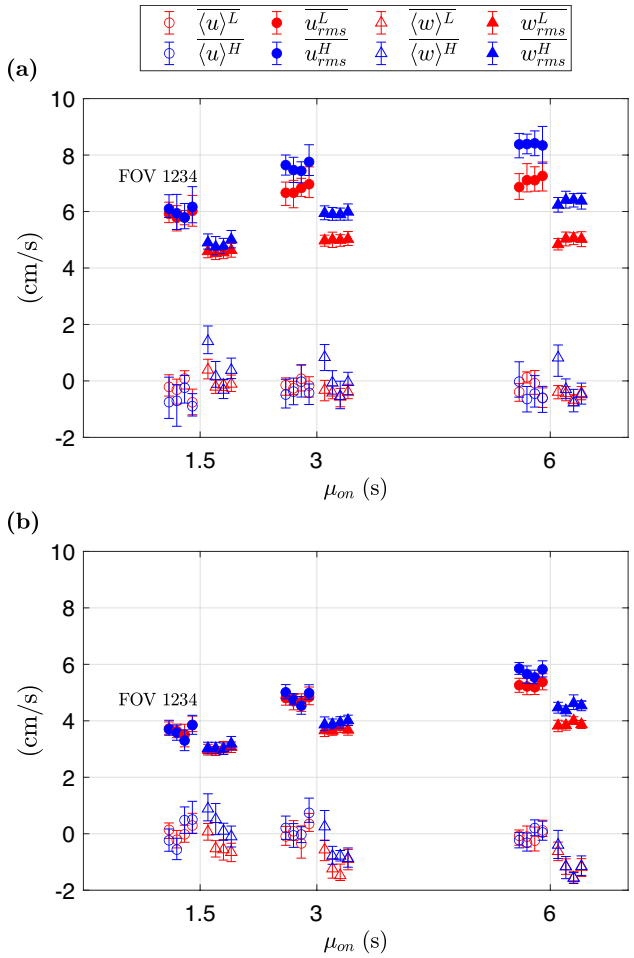

Fig. 8 Summary of one-point statistics in the homogeneous region $|x| < 10$ cm as a function of $\mu_{\mathrm{on}} = [1.5, 3, 6]$ s, for the grid attachment (**a**) and the cylinder attachment (**b**). The source fraction is illustrated by different colors, red ($\phi = 6.25\%$) and blue ($\phi = 12.5\%$). Data from u and w are depicted respectively on the left and right side of the corresponding μ_{on}. Data for FOVs1–4 for the same mean on-time are displayed by offsetting them with respect to each other (left to right), as shown by the text. The error bars illustrate the spatial variability of each quantity, displaying 95% of the range

Simple scaling arguments would suggest that the RMS velocities would scale with the jet velocity (u_{rms}, w_{rms}) $\sim U_J$ (Dou et al. 2016; Hoffman and Eaton 2021; Tan et al. 2023). This expectation is indeed borne out in the fact that the cylindrical attachment reduces the RMS velocities. However, the simple scaling is not sufficient to explain the fact that the RMS velocities are sensitive to ϕ and μ_{on} for random-jet-stirred flow as discussed in Sect. 2.

Figure 8 shows that $\phi = 12.5\%$ produces higher RMS velocities than $\phi = 6.25\%$, suggesting that the previously found value of $\phi_{\mathrm{optimal}} = 12.5\%$ appears to be robust with respect to adding more jet arrays. To understand how the RMS velocities vary with μ_{on} in our experimental setup, we use the knowledge gained from the single jet data (Sect. 4.1):

The axial velocity of an individual jet at the tank center increases with the pump on-time up to the point where it resembles a continuous jet and the velocity values at on-times below this point are lower than the continuous jet value mainly due to the diffusion of momentum in the pulsed jet flow. Thus, the RMS velocity in random-jet-stirred turbulence must scale with the jet exit velocity compensated by the velocity decay with distance from canonical turbulent round jets (Eq. 4). In other words, $u_{\mathrm{rms}} \sim U_J D_J/(\frac{1}{2}L_A)$, and the correct way to make the RMS velocity dimensionless is $(u_{\mathrm{rms}}\frac{1}{2}L_A)/U_J D_J$. Here, we have neglected the influences of the virtual origin (x_0) and the precise value of the velocity decay constant (B) for simplicity. Further, the importance of the jet momentum diffusion suggests that the correct way to make the mean on-time dimensionless is to use the jet exit velocity and tank size: $U_J\mu_{\mathrm{on}}/(\frac{1}{2}L_A)$ (i.e., the second option in Eq. (1)).

In order to demonstrate this relationship between u_{rms} and μ_{on}, we use single-point data measured by ADV at the tank center. In these data, we modified $\frac{1}{2}L_A$ and μ_{on} at a constant source fraction (12.5%) and jet exit conditions (grid attachment). The results are summarized in Fig. 9 and Table 3. We observe scatter in the dimensional data that collapses reasonably well when made dimensionless (Fig. 9). Overall, the RMS velocities increase with dimensionless mean on-time up to $U_J\mu_{\mathrm{on}}/(\frac{1}{2}L_A) \approx 4$, but saturate for further increases of μ_{on} or decreases of L_A. (Note Carter et al. 's (2016) data also show a saturation of turbulence intensity at $U_J\mu_{\mathrm{on}}/(\frac{1}{2}L_A) \approx 4$). Fig. 9 also corroborates that the RMS velocities scale as $u_{\mathrm{rms}} \sim U_J D_J/(\frac{1}{2}L_A)$ since $(u_{\mathrm{rms}}\frac{1}{2}L_A)/(U_J D_J)$ is an $O(1)$ quantity. Physically, we interpret these results as stating that an increase in μ_{on} in a given tank geometry results in higher intensity turbulence at the tank center, but this effect saturates when μ_{on} is high enough such that each pulsed jet produces a flow similar to its continuous jet equivalent. Thus, the turbulence intensity is determined by both the jet characteristics and the decay of its momentum with distance from the nozzle.

4.2.5 Scales of motion: integral scale and Taylor scale

To estimate the different length scales of turbulence, we use the two-point autocorrelation

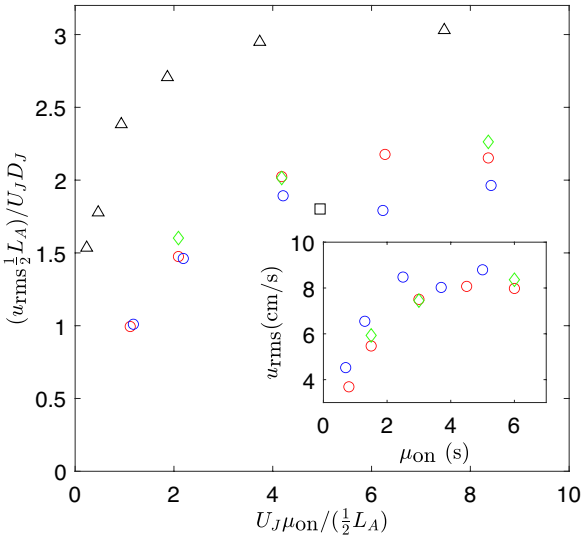

Fig. 9 Variation of u_{rms} with respect to μ_{on} in dimensionless (main plot) and dimensional (inset) terms, from ADV data (circles) and PIV data averaged over the homogeneous turbulence region (diamonds). Distance from the pump exit to the tank center varies: $\frac{1}{2}L_A = 59.0$ cm for red and green markers and $\frac{1}{2}L_A = 48.5$ cm for blue markers. Data from Carter et al. (2016) are shown with black triangle markers and data from Esteban et al. (2019) are shown with a black square. The source fraction is $\phi = 12.5\%$ for all data

$$\rho_{ij}(r) = \frac{\langle u_i'(\boldsymbol{x}) \cdot u_i'(\boldsymbol{x} + r\boldsymbol{e_j})\rangle}{u_{i,\mathrm{rms}}^2}, \tag{8}$$

where r is the spatial lag in the direction given by the unit vector $\boldsymbol{e_j}$. This computation is conducted in the homogeneous turbulence region.

Before analyzing the turbulence scales, we check that combining data from the two cameras does not introduce significant errors. The discrepancy between the autocorrelation functions in the homogeneous region measured by Camera 1 ($-10 < x < 0$ cm) and by Camera 2 ($0 < x < 10$ cm) are less than 5% different from the autocorrelation function calculated by combined data from Camera 1 and 2 ($-10 < x < 10$ cm). Thus, we use the velocity fields from both cameras to compute the autocorrelation, which expands the spatial lag in the x direction.

Figure 10a shows the autocorrelation functions for the GrHi30 case at FOV2. We can see that despite combining data from both cameras, we do not have the required

Table 3 Summary of experimental condition and parameters via ADV measurements

$\frac{1}{2}L_A$ (cm)	59.0					48.5				
μ_{on} (s)	0.8	1.5	3.0	4.5	6.0	0.7	1.3	2.5	3.7	5
u_{rms} (cm/s)	3.69	5.47	7.50	8.07	7.98	4.52	6.55	8.48	8.02	8.79
$U_J\mu_{\mathrm{on}}/(\frac{1}{2}L_A)$	1.12	2.09	4.18	6.27	8.36	1.18	2.19	4.21	6.23	8.42
$(u_{\mathrm{rms}}\frac{1}{2}L_A)/U_J D_J$	0.99	1.29	1.78	1.91	1.89	1.01	1.46	1.89	1.79	1.96

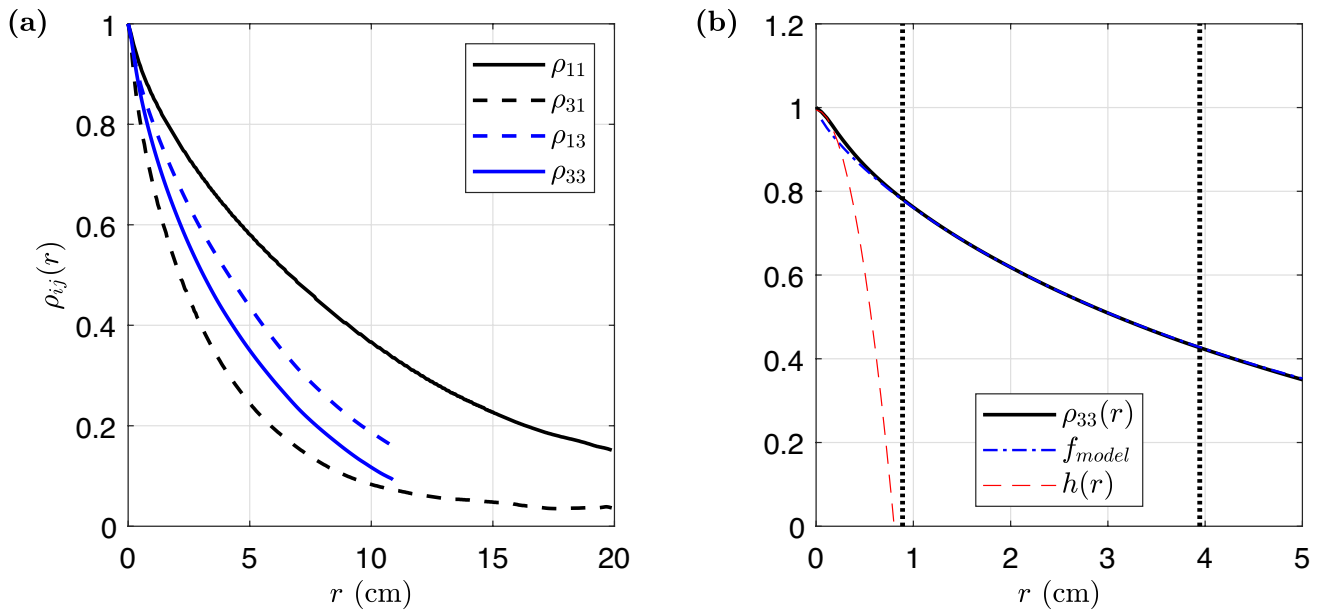

Fig. 10 Autocorrelation functions for the GrHi30 case at FOV2 (**a**) and the z direction longitudinal autocorrelation function with the model function for the inertial subrange and the parabolic fit at the origin (**b**). The dotted lines are the lower and upper bound of the inertial subrange

measurement volume to measure the autocorrelation to its first zero-crossing and evaluate the integral length scale directly as $L_{ij} = \int_0^\infty \rho_{ij}(r)dr$. Instead, we estimate the integral length scales by fitting a model function to ρ_{ii} in the inertial subrange

$$f_{\text{model}}\left(\frac{r}{L^M}\right) = \frac{2}{\Gamma(q)}\left(\frac{r}{2L^M}\alpha\right)^q K_q\left(\frac{r}{L^M}\alpha\right) \tag{9}$$

where $\alpha = \sqrt{\pi}\Gamma(q+\frac{1}{2})/\Gamma(q)$, Γ is the gamma function, and K_q is the modified Bessel function of the second kind (Pope 2000). The model function has two fitting parameters, q and L^M, where the superscript M refers to the fact the integral scale is computed fitting data to the model Eq. (9). Figure 10b shows that the model function fits ρ_{33} very well in the inertial subrange (determined from plateaus of the compensated second-order structure functions as described below).

For completeness, we also calculate the integral length scales by fitting an exponential curve to the autocorrelation functions, $f_{\text{exp}} = \exp(-x/L^F_{ij})$. The superscript F refers to the fact that the integral scale is calculated from a fit the exponential function. The differences between L^M_{ii} and L^F_{ii} are less than 15%.

Figures 11 and Table 4 summarize the various integral scales. We observe again that the values are very similar at different FOVs for the same experimental condition which shows the turbulence is homogeneous. Across all FOVs and experimental conditions, L^M_{11} is always larger than L^M_{33} and

Table 4 Two-point turbulence statistics in the homogeneous region at FOV2

Case	L^M_{11} cm	L^M_{33}	L^F_{11}	L^F_{31}	L^F_{13}	L^F_{33}	λ_z mm	T_{wz} s	$\langle\epsilon\rangle$ cm^2/s^3	η mm	u_η mm/s	τ_η ms	Re_λ ($\times 10^2$)	Re_L ($\times 10^3$)
GrLo15	8.4	4.2	7.8	3.1	4.8	3.8	6.7	0.9	11	0.16	5.7	27	3.4	2.0
GrLo30	11	5.0	9.8	3.5	5.9	4.6	6.8	0.9	14	0.15	6.0	25	3.8	2.6
GrLo60	14	5.3	12	3.8	6.5	5.0	7.0	1.0	14	0.15	5.9	26	4.0	2.9
GrHi15	7.3	4.2	7.3	2.9	4.4	3.9	6.5	0.8	14	0.15	6.0	25	3.5	2.1
GrHi30	9.2	5.0	8.3	3.7	5.4	4.8	6.4	0.8	22	0.13	6.7	20	4.2	3.2
GrHi60	11	5.9	10	4.7	6.8	5.5	6.6	0.9	25	0.13	6.9	19	4.7	3.9
CyLo15	8.1	4.6	7.3	3.3	4.5	4.4	8.4	1.5	3.2	0.21	4.1	52	2.8	1.5
CyLo30	11	5.8	9.8	4.4	6.0	5.3	8.3	1.5	5.1	0.19	4.6	41	3.4	2.2
CyLo60	14	6.4	12	4.4	7.4	5.7	8.4	1.5	5.5	0.19	4.7	40	3.7	2.5
CyHi15	6.9	5.2	6.7	3.3	4.4	4.4	8.3	1.5	3.5	0.21	4.2	50	2.8	1.5
CyHi30	9.5	5.7	8.5	4.0	5.6	5.0	8.0	1.3	6.3	0.18	4.9	38	3.5	2.2
CyHi60	11	7.2	10	4.7	6.5	5.6	7.8	1.3	8.2	0.17	5.2	33	3.9	2.8

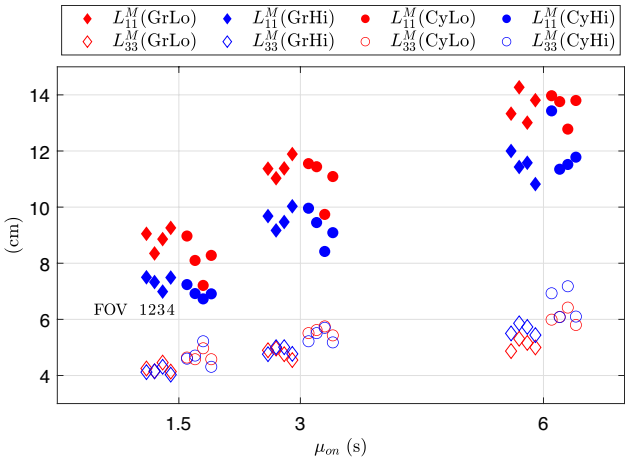

Fig. 11 Longitudinal integral length scales estimated by the model function as a function of $\mu_{\text{on}} = [1.5, 3, 6]$ s. Quantities for the grid and cylinder cases are located left and right sides of the corresponding μ_{on}, respectively. Different source fractions are represented by red ($\phi = 6.25\%$) or blue ($\phi = 12.5\%$) color. Data for FOVs1–4 for the same mean on-time are displayed by offsetting them with respect to each other (left to right), as shown by the text

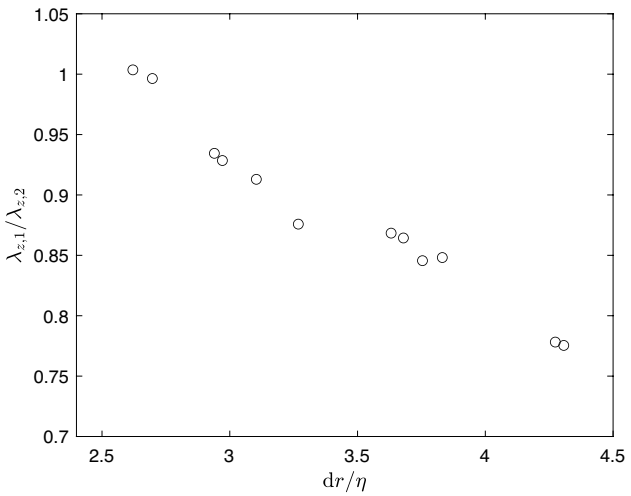

Fig. 12 Ratio of λ_z calculated using Eq. (11) (λ_{z1}) and by fitting Eq. (10) to the longitudinal autocorrelation function (λ_{z2}) as a function of $\mathrm{d}r/\eta$. The data are averaged across all FOVs

$L_{11}^F > L_{13}^F > L_{33}^F > L_{31}^F$, which is consistent with the large-scale anisotropy discussed above. Additionally, lower ϕ and/or higher μ_{on} yield larger L_{11}^M, while L_{33}^M appears to be insensitive to ϕ and only a function of μ_{on}. The cylindrical attachment has little effect on L_{11}^M, but does increase L_{33}^M slightly.

The simplest scaling argument to predict the integral scale for random-jet-stirred turbulence states that $L \sim D_J$ (Carter et al. 2016; Hoffman and Eaton 2021; Tan et al. 2023) since all scales of motion in a canonical jet scale with the jet diameter. Focusing on L_{33} as the most representative measure of the largest turbulent motions, we see evidence to support this argument since the cylindrical attachment, which widens the jet and creates a larger effective jet diameter, consistently produces a larger integral scale compared to the grid attachment. The scaling of the integral scale with the (effective) jet diameter is also supported by the fact that L is insensitive to changes in ϕ. There is a slight increase of L_{33} with mean on-time, but this is much more pronounced for the integral scale in the jet-axial direction L_{11}. Focusing on L_{11}, this scale is expected to more sensitive to the mean on-time as it is also related to the characteristic length associated with an individual jet pulse, $\mu_{\text{on}}(U_J D_J/(\frac{1}{2}L_A))$. However, unlike the RMS velocities, we do not necessarily observe a clear saturation point of the integral length scales.

The Taylor microscale λ can be calculated from its definition by fitting an osculating parabola

$$h(r) = 1 - r^2/\lambda^2, \tag{10}$$

to the autocorrelation function near the origin, or it can be calculated via the relation

$$\lambda_z = w_{\text{rms}}\sqrt{30\nu/\langle\epsilon\rangle}, \tag{11}$$

by assuming small-scale isotropy (Pope 2000). Here, $\langle\epsilon\rangle$ is the mean turbulent kinetic energy dissipation rate obtained from the compensated structure function as discussed below (hereafter we refer to this simply as mean dissipation rate). We follow both methods, where we fit Eq. (10) to the first 2 points of the autocorrelation function excluding the point at $r = 0$ (Fig. 10b), and compare the results from both methods as a function of the spatial resolution ($\mathrm{d}r$) of the data in Fig. 12. While both methods yield the same answer when the flow field is resolved to approximately 2.5η (where η is the Kolmogorov microscale and discussed more below), fitting a parabola to the autocorrelation data overestimates the Taylor scale when the data are less well resolved. Hence, we report λ_z, calculated from Eq. 11 using FOV2 data, in Table 4.

4.2.6 Scales of motion: inertial subrange and dissipation scales

To examine the flow statistics in the inertial and dissipation subranges, we use the second-order structure functions

$$D_{ij}^2(r) = \langle\overline{(u_i'(\boldsymbol{x} + r\boldsymbol{e_j}) - u_i'(\boldsymbol{x}))^2}\rangle, \tag{12}$$

computed with data from both cameras in the homogeneous turbulence region. Averaging is first conducted over the

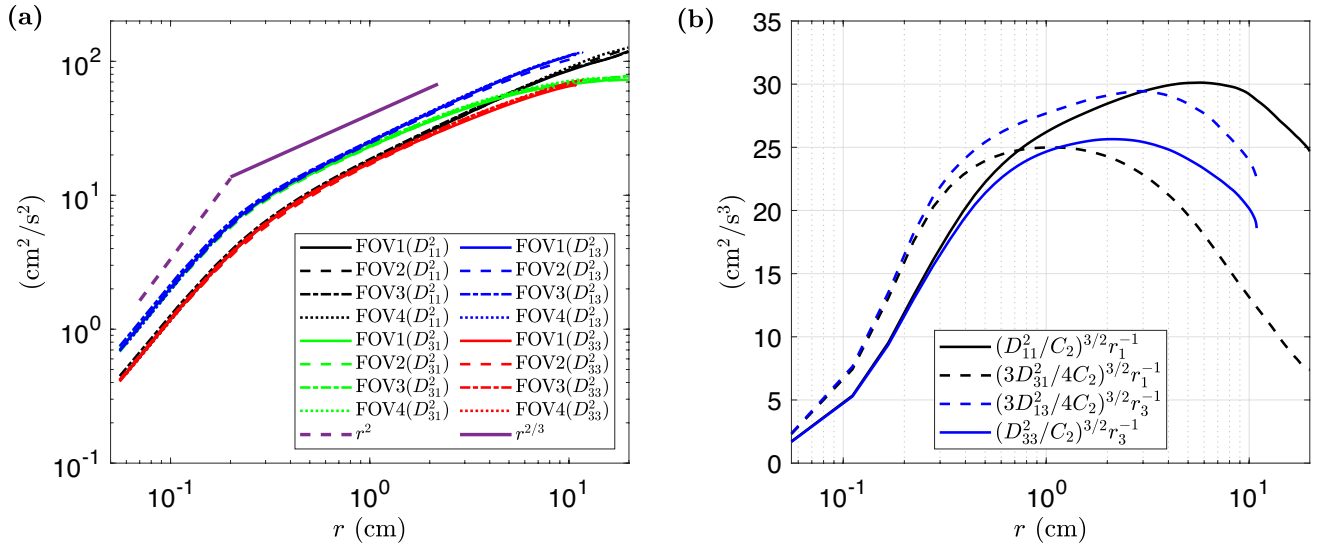

Fig. 13 Second-order structure functions for the GrHi60 case across different FOVs (**a**) and the corresponding compensated structure functions at FOV2 (**b**)

homogeneous turbulence region in each velocity measurement and then over the entire set of measurements.

Figure 13 shows the second-order structure functions in the GrHi60 case, which serves as a representative example for all cases for scaling behavior. We see that the data show the expected power-law scaling in the dissipation range ($\sim r^2$) and in the inertial subrange ($\sim r^{2/3}$). We can also extract information on the degree to which the flow is homogeneous and isotropic across scales. For this, the GrHi60 case is a worst-case example since it has the highest μ_{on}. In terms of homogeneity, Fig. 13a shows that there is little-to-no variation between data at different FOVs (lines of the same color overlap with each other), allowing us to conclude that the flow is homogeneous across all scales. In terms of isotropy, Fig. 13a shows that the longitudinal (D_{11}^2 and D_{33}^2) and transverse (D_{31}^2 and D_{13}^2) structure functions calculated using different velocity components overlap with each other, respectively, for $r \lesssim 1$ cm and do not deviate too far from each other for $r \lesssim 3$ cm. In Fig. 13a, which shows the compensated structure function data at FOV2, we can see more clearly that the dissipation range scales are very isotropic and that the inertial subrange scales are reasonably isotropic. Clearly, the large-scale flow which has anisotropic features becomes more isotropic down the turbulence energy cascade, as expected from classical Kolmogorov theory.

To identify the extent of the inertial subrange and also estimate the mean dissipation rate ($\langle\epsilon\rangle$), we apply the Kolmogorov similarity hypotheses which predict that the longitudinal and transverse structure functions are uniquely determined by $\langle\epsilon\rangle$

$$D_{ii}^2(r) = C_2(\langle\epsilon\rangle r)^{2/3}, \tag{13a}$$

$$D_{ij}^2(r) = \frac{4}{3}C_2(\langle\epsilon\rangle r)^{2/3}\ (i \neq j), \tag{13b}$$

with $C_2 = 2.0$ being the Kolmogorov constant (Pope 2000). From the compensated structure functions (such as the GrHi60 case at FOV2 shown in Fig. 13b), we identify the extent of the inertial subrange as the range where the compensated structure function is within 5% of its maximum. Figure 13b shows that we obtain a much cleaner and clearer plateau in the D_{33}^2 data compared with the D_{11}^2 data, which show a narrow plateau at larger scales that overlap with our estimates of the integral scale. We interpret this as suggesting that the flow forcing from the jets pumps extra energy into the u component of velocity at scales within the turbulent energy cascade.

To evaluate $\langle\epsilon\rangle$, we average the compensated D_{33}^2 data by inverting the relation in Eq. (13) over the inertial subrange, as this method has been shown to be more robust than others $\langle\epsilon\rangle$De Jong et al. 2009). These values of $\langle\epsilon\rangle$ are summarized in Table 4. As a check of the sensitivity, we also compute $\langle\epsilon\rangle$ using D_{31}^2 data and the standard formulations

$$\langle\epsilon\rangle = C\frac{u_{\mathrm{rms}}^3}{L_{11}^F}, \quad \langle\epsilon\rangle = C\frac{w_{\mathrm{rms}}^3}{L_{33}^F} \tag{14}$$

where $C = 0.5$.

Figure 14 presents a comparison of $\langle\epsilon\rangle$ under different experimental conditions. There is clear evidence for homogeneity in how similar the values of $\langle\epsilon\rangle$ are across different FOVs. Additionally, the values obtained from the D_{33}^2 data closely match the values obtained from Eq. (14) (Fig. 14) and the values obtained from the D_{31}^2 (not shown).

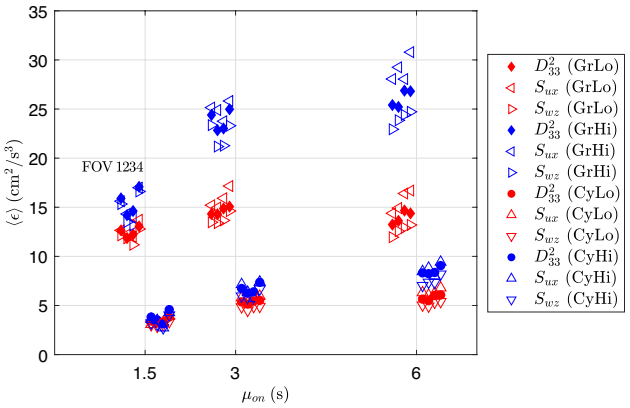

Fig. 14 Summary of mean dissipation rate estimated from the structure function (D_{33}^2) and the scaling method, denoted as $S_{u_i x_j}$, as a function of $\mu_{\text{on}} = [1.5, 3, 6]$ s. Subscripts of S represent the velocity and coordinate components chosen for the calculation. Quantities for the grid and cylinder cases are located left and right sides of the corresponding μ_{on}, respectively. The color symbols indicate the different levels of the source fraction (red: $\phi = 6.25\%$ and blue: $\phi = 12.5\%$). Data for FOVs1–4 for the same mean on-time are displayed by offsetting them with respect to each other (left to right), as shown by the text

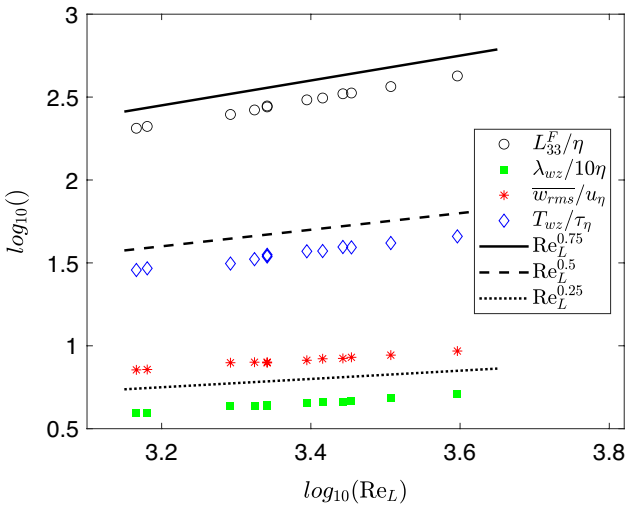

Fig. 15 Largest-to-smallest scale ratio regarding turbulence Reynolds number at FOV2. Values are shown as log scale to illustrate the exponential scaling relation. Note the values for λ_z/η are plotted a decade smaller for easier visualization

The data in Fig. 14 also show that $\langle\epsilon\rangle$ increases with higher ϕ and/or longer μ_{on}, with the cylinder attachment decreasing the mean dissipation rate relative to the grid attachment. Since the data show that the scaling relationship in Eq. (14) accurately predicts the mean dissipation rate, we can extrapolate the previously found scaling relationships for the RMS velocities ($u_{\text{rms}} \sim U_J D_J/(\frac{1}{2}L_A)$) and the integral scales ($L \sim D_J$), which gives $\langle\epsilon\rangle \sim U_J^3 D_J^2/(\frac{1}{2}L_A)^3$. This relationship predicts $\langle\epsilon\rangle$ as 19.16 cm^2/s^3 for the grid attachment, which is close the values reported in Fig. 14. The prediction for the cylinder attachment cases is similarly close to the calculated values. Applying our predicted relationship to previous data, we find a value of 0.29 m^2/s^3 for Carter et al. (2016) and 15 cm^2/s^3 for Esteban et al. (2019), while the reported values are 0.1–1.2 m^2/s^3 and 14.6 cm^2/s^3, respectively. The favorable comparison between the predicted and reported values indicates that the scaling $\langle\epsilon\rangle \sim U_J^3 D_J^2/(\frac{1}{2}L_A)^3$ is able to predict the mean dissipation rate within an order of magnitude, and sometimes much better.

While our scaling prediction for the mean dissipation rate depends solely on the jet properties and tank size, we do also observe a small increase with increasing μ_{on} with a hint of saturation for $U_J\mu_{\text{on}}/(\frac{1}{2}L_A) \gtrsim 4$. The source fraction ϕ also has an impact on the mean dissipation rate since it controls the total energy input that must be dissipated to maintain stationary turbulence.

Using the estimated $\langle\epsilon\rangle$ from D_{33}^2 data, the Kolmogorov microscales are calculated via the relations

$$\begin{aligned} \eta &= (\nu^3/\langle\epsilon\rangle)^{1/4}, \\ u_\eta &= (\nu\langle\epsilon\rangle)^{1/4}, \\ \tau_\eta &= (\nu/\langle\epsilon\rangle)^{1/2}, \end{aligned} \tag{15}$$

where η, u_η and τ_η are the Kolmogorov length, velocity, and time scales, respectively. These values are reported in Table 4.

4.2.7 Scale separation as a function of Reynolds number

High Reynolds number turbulent flows have a large separation between the largest and smallest scales. We inspect this dependency in our data by comparing it with the scaling laws

$$\frac{L_0}{\eta} \sim \mathrm{Re}_L^{3/4}, \ \frac{\lambda}{\eta} \sim \mathrm{Re}_L^{1/4}, \ \frac{u_0}{u_\eta} \sim \mathrm{Re}_L^{1/4}, \ \frac{T_0}{\tau_\eta} \sim \mathrm{Re}_L^{1/2}, \tag{16}$$

where L_0, u_0, T_0 are the largest characteristic scales of length, velocity, and time, respectively, and $\mathrm{Re}_L = u_0 L_0/\nu$ is the Reynolds number based on these scales (Pope 2000). Using $L_0 = L_{33}^F$, $u_0 = \overline{w_{\text{rms}}}$, and $T_0 = T_{wz} = L_{33}^F/\overline{w_{\text{rms}}}$, this Reynolds number becomes $\mathrm{Re}_L = \overline{w_{\text{rms}}} L_{33}^F/\nu$. Figure 15 shows the comparison of the ratio of the largest to smallest scales as a function of Re_L for all experimental conditions at FOV2, where we observe that the data show a very high degree of correlation with the expected scaling laws (R^2 values greater than 0.95). We note that the scale separations do not follow

the expected scaling laws if we choose scales from the horizontal direction (e.g., $\overline{u_{\rm rms}}$, L_{11}^F), which is presumably due to the fact that the signatures of jet pulses cause the flow to deviate from the ideal turbulence.

In idealized turbulence studies, the Taylor scale Reynolds number is more commonly used. We define it here as $\mathrm{Re}_\lambda = \overline{w_{\rm rms}}\lambda_z/\nu$, choosing the vertical characteristic velocity and length scales as before. Re_λ falls in the range 340–470 for the grid attachment, and 280–390 for the cylinder attachment (Table 4).

While it is common for laboratory studies to report a Taylor scale Reynolds number, it is often difficult to directly compare Reynolds number effects across studies since different stirring mechanisms and different methods for calculating the Reynolds number can lead to differences in the scale separation for the same Reynolds number. Thus, in Fig. 16a we show the compensated longitudinal structure function for different cases and compute the scale separation observed in the inertial subrange. Figure 16b shows how this scale separation varies with our reported Re_λ. We find that our scale separation is very similar in magnitude to standard DNS of turbulence in a cubic periodic box (Ishihara et al. 2009), which makes it easier to compare across laboratory experiments and DNS at similar Reynolds numbers.

4.2.8 Jet signatures and forcing timescales

In Sect. 4.2.1 and Fig. 6, we found that the turbulence becomes homogeneous at a distance of approximately $4J$ from the jet arrays suggesting that the jets have merged in a statistical sense. Here, we investigate jet merging further and show how jet signatures can still be periodically detected in the homogeneous turbulence region (e.g., Fig. 4a).

If individual jet signatures appear in the otherwise homogeneous turbulence region, they should produce peaks in turbulent velocity power spectra. We calculate the spectra from the velocity data measured by ADV to investigate this. To reduce the statistical uncertainty, the 30-minute time series are divided into six subsamples of five minutes each, with spectra calculated from subsamples and then ensemble-averaged to obtain the final result.

Figure 17 shows spectra for different $\frac{1}{2}L_A$ and $\mu_{\rm on}$. When plotted as a function of dimensional frequency (panels a and c), it can be seen that an increase in $\mu_{\rm on}$ first leads to an increase in the spectral energy density at all scales (blue line → red line). However, further increases of $\mu_{\rm on}$ do not affect the spectral energy density in the inertial subrange, but produce a peak at $f(\mu_{\rm on}+\mu_{\rm off}) \approx 1$ (observed more clearly in the linear scale in panels b and d), which corresponds to the jet forcing timescale, $\tau_{F1} = \mu_{\rm on} + \mu_{\rm off}$ (option 1 in Eq. (3)). No peaks are observed at frequencies associated with $\tau_{F2} = \mu_{\rm on}$ and $\tau_{F3} = \phi\mu_{\rm on}$ (the other options in Eq. (3)), suggesting that neither of these is the correct candidate for the forcing timescale.

Examining the data in Fig. 17, where we have varied $\mu_{\rm on}$ and L_A independently, we note that the spectral peak at $f(\mu_{\rm on}+\mu_{\rm off}) \approx 1$ only occurs for $U_J\mu_{\rm on}/(\frac{1}{2}L_A) \gtrsim 4$. This further highlights the importance of the dimensionless mean on-time: it not only predicts the saturation of the RMS velocities, but it also predicts the signature of individual jets observed in the region of otherwise statistically homogeneous turbulence. Physically, we interpret this as individual

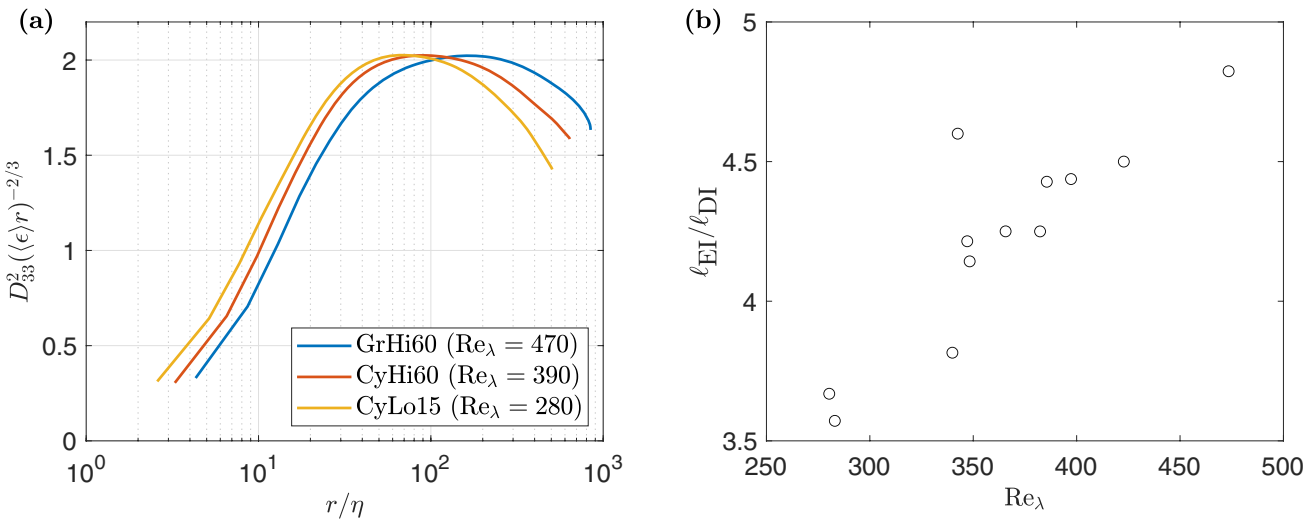

Fig. 16 Normalized D_{33}^2 for different Re_λ (**a**), and the extent of the inertial subrange as measured by $\ell_{\rm EI}/\ell_{\rm DI}$ as a function of Re_λ (**b**). $\ell_{\rm EI}$ and $\ell_{\rm DI}$ are the scales demarcating the energy-containing and inertial ranges, and inertial and dissipative ranges, respectively

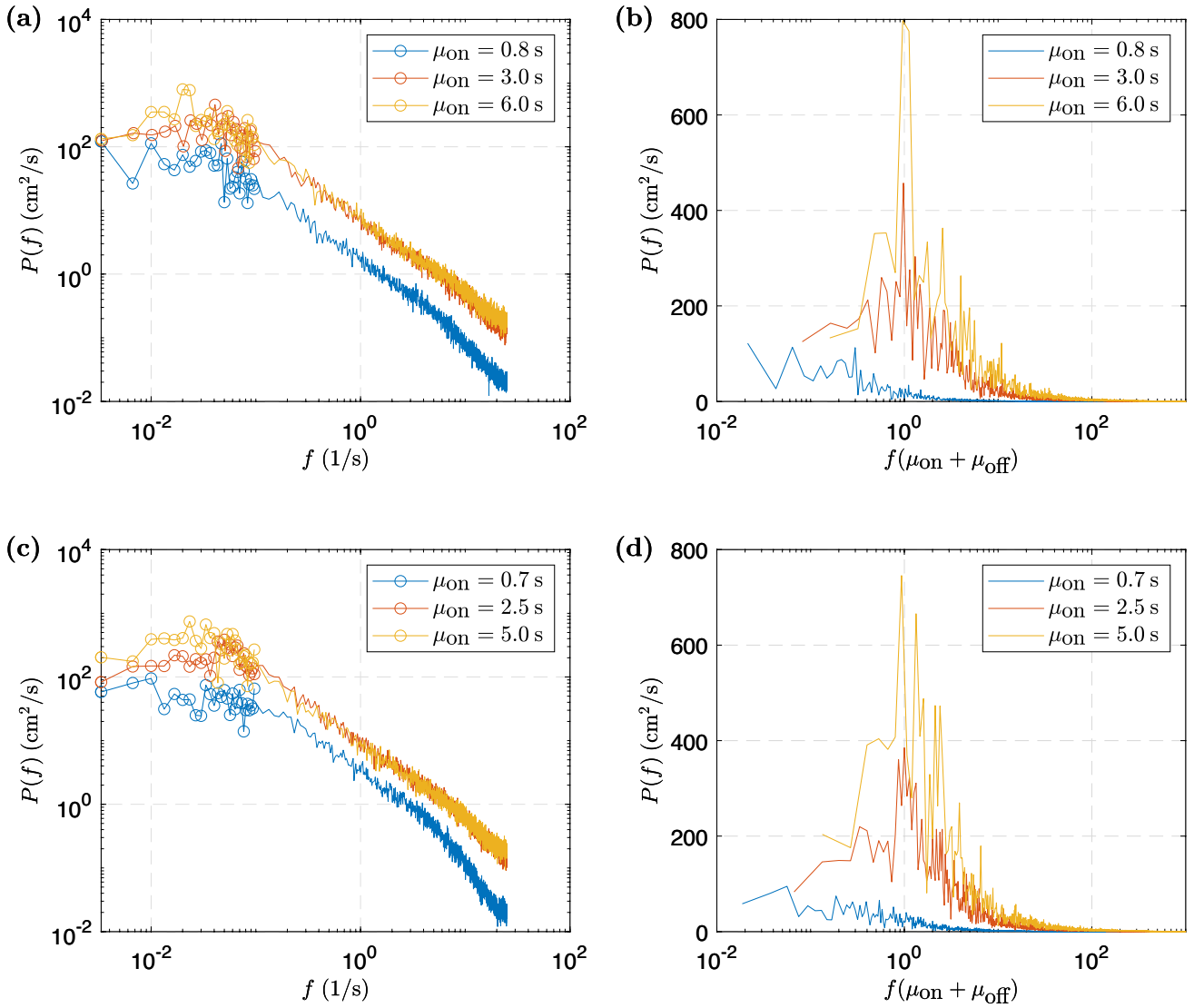

Fig. 17 Turbulent velocity spectra with $\frac{1}{2}L_A = 59.0$ cm (a and b) and $\frac{1}{2}L_A = 48.5$ cm (c and d). Spectra are plotted as a function of dimensional frequency on logarithmic scales in panels (**a**) and (**c**), while they are plotted as a function of dimensional frequency in log-linear coordinates to emphasize the spectral peak in panels (**b**) and (**d**). In panels a and c, the low-frequency spectra are plotted at every data point while only every 20th data point is plotted in the higher-frequency region for clarity. In panels (**a**) and (**b**), $U_J\mu_{on}/(\frac{1}{2}L_A) = 1.12, 4.18$, and 8.36 for $\mu_{on} = 0.8, 3$, and 6 s, respectively. In panels (**c**) and (**d**), $U_J\mu_{on}/(\frac{1}{2}L_A) = 1.18, 4.21$, and 8.42 for $\mu_{on} = 0.7, 2.5$, and 5 s, respectively

jet pulses overpowering the background turbulence, which prevents them from becoming fully mixed.

4.3 Comparison of symmetric forcing configurations: Two *vs.* four jet arrays

We now turn towards investigating the effect of different array geometries, namely comparing the turbulence produced by using only two-facing arrays in our setup with the turbulence produced by using all four jet arrays. Turbulence characteristics of interest are TKE, isotropy (u_{rms}/w_{rms}), and Reynolds number. We use ADV data, and as before, we use the vertical velocity to compute the Reynolds number as $\mathrm{Re}_{L,\mathrm{ADV}} = w_{rms}^2 T_{I,w}/\nu$, where $T_{I,w}$ is the integral time scale estimated from the autocorrelation function up to the first zero-crossing.

Table 5 shows the turbulence characteristics data. Four jet arrays provide better performance than two-facing arrays in terms of a higher turbulence intensity and a larger Reynolds number. This is because, for the given tank geometry and source fraction, the additional arrays provide more large-scale forcing. Furthermore, four jet arrays create a more

Table 5 Comparison of turbulent characteristics for two-facing and four jet arrays configurations. All data are for $\phi = 12.5\%$

	Two-facing arrays			Four jet arrays		
μ_{on} (s)	1.5	3	6	1.5	3	6
k (cm^2/s^2)	35.76	46.27	44.67	32.20	62.42	72.34
M_1 ($\times 10^{-2}$)	3.26	3.59	7.20	10.83	3.31	4.39
$\mathrm{Re}_{L,\mathrm{ADV}}$ ($\times 10^3$)	1.47	1.58	1.64	1.56	3.20	5.41
$u_{\mathrm{rms}}/w_{\mathrm{rms}}$	1.60	1.79	1.87	1.36	1.41	1.42

isotropic turbulent flow, since jet flows from one array are more likely to lose their signature by interacting with the jet flows perpendicular to that array. Note that the exception observed in the cases with $\mu_{on} = 1.5$ s, where the two-facing arrays exhibit higher TKE, can be attributed to the stronger secondary mean flow developed in the tank center as characterized by higher M_1 values.

5 Conclusions

Within the context of a new facility, where we generate random-jet-stirred turbulence in a vertical octagonal prism-shaped tank using four jet arrays on four faces of the tank, we have studied high-Reynolds-number turbulence with a negligible mean flow and mean shear that is homogeneous over a large domain (2.5–4L in the horizontal direction and 5–8L in the vertical direction). The tank design ensures that the flow is isotropic in horizontal planes due to jet forcing from four directions, but this dominance of forcing in the horizontal direction also leads to anisotropy at the largest scales and an excess of horizontal momentum in the turbulent scales of motion. By investigating the properties of the turbulence at different scales, we find that anisotropy at large scales decays to produce scale-local isotropic turbulence within the inertial subrange and dissipation range, with the isotropy improving with decreasing scale. We can also control the Reynolds number and scales of turbulent motion (RMS velocities, integral scales, and dissipation rate) to varying degrees by changing the parameters of the jet driving algorithm. By examining the ratio of integral-to-Kolmogorov scales and span of the inertial subrange, we confirm that the flow statistics obey the expected scaling relationships for scale separation as a function of Reynolds number for idealized turbulence.

As noted in Sect. 1, laboratory facilities using randomized stirring from multiple units (e.g., jets, impellers) produce turbulence that has a smaller mean flow and better homogeneity and isotropy over a larger region compared with facilities that use continuous stirring, usually at the cost of lower turbulence intensity and Reynolds number. Additionally, the complexity introduced by randomized stirring also means that it becomes more difficult to predict the scales of turbulence as a function of the flow from each stirring unit, tank size, and the algorithm that drives the units. In this regard, we have made a number of steps forward that we summarize below.

We tested how manipulating the properties of each jet by installing 3D-printed attachments to the jet exit affects the jet flow, including a grid attachment to provide flow conditioning and a horizontal cylindrical attachment to induce unsteady flow separation and additional vertical mixing. We observed that the grid attachment successfully conditioned the flow so that the jet flow was close to a canonical non-swirling turbulent round jet. The cylindrical attachment induced a wake in the near-field that introduced more vertical mixing, but in the far field the flow relaxed to produce a wider and slower jet velocity profile. Notably, the ratio of the normal fluctuations (w_{rms}) to the axial fluctuations (u_{rms}) was similar for both attachments in the far field, and thus, the cylindrical attachment yielded only modest gains in flow isotropy in the tank center. Interestingly, we also found that the integral scale increased slightly for the cylindrical attachment, which we attribute to a wider effective jet diameter. Overall, we find that jet exit attachments could be used to reduce the jet exit velocity and increase the effective jet diameter.

Based on detailed analysis of turbulence from a wide range of tests, we provide scaling predictions for the relevant scales of turbulent motion based on the characteristics of individual jets, tank geometry, and parameters of the algorithm that controls the jet arrays. In particular, we find $u_{\mathrm{rms}} \sim U_J D_J/(\frac{1}{2}L_A)$, $L \sim D_J$, and $\langle\epsilon\rangle \sim U_J^3 D_J^2/(\frac{1}{2}L_A)^3$. These scalings indicate that turbulence in our random-jet-stirred tank is primarily controlled by the properties of the individual jets and the diffusion of their momentum with distance from the nozzle. Additionally, the mean on-time μ_{on} plays a critical role in determining whether the discharged pulses exhibit continuous-jet-like properties—it does so for $U_J\mu_{on}/(\frac{1}{2}L_A) \gtrsim 4$. We found that increasing μ_{on} above this level does not result in further increases of turbulent intensity, but rather produces a peak in the velocity spectra at a frequency related to the jet forcing timescale $f(\mu_{on} + \mu_{off}) \approx 1$, suggesting that the jet pulses are not fully mixed with the background turbulence. The source fraction ϕ also affects the overall intensity of the background turbulence as it determines the fraction of jets that are active at

any given time, with larger ϕ values producing larger u_{rms} and $\langle\epsilon\rangle$ within the limits of our tests.

While most facilities use one or two-facing arrays, we have found that the addition of two more arrays has several benefits. We are able to achieve a higher turbulence intensity and Reynolds number with improved isotropy. We are also able to reduce the 'statistical jet merging distance' (defined here as the minimum distance from each array where the turbulence is homogeneous) from $L_{\mathrm{JM}} \approx 6J$ (where J is the inter-jet spacing) as previously found to $L_{\mathrm{JM}} \approx 4J$. This is believed to be due to the arrangement of jet arrays that are perpendicular to each other, which merge with the surrounding flow at a shorter distance. This can be important since the jet merging distance is one of the considerations when designing the tank size.

Finally, in random-jet-stirred turbulence, the sunbathing algorithm drives the jets in pulsed mode with a mean on-time μ_{on}, but this mean on-time has usually been reported in dimensional terms (Variano and Cowen 2008; Pérez-Alvarado et al. 2016; Carter et al. 2016) and the nature of the pulsed jet flow had not been previously investigated. We introduced two possible dimensionless mean on-times: (1) based on the jet exit velocity and jet diameter, $U_J\mu_{\mathrm{on}}/D_J$; and (2) based on the jet exit velocity and the travel distance to the tank center, $U_J\mu_{\mathrm{on}}/(\frac{1}{2}L_A)$. Measurements of the near-field flow from an individual jet operated in pulsed mode with an on-time corresponding to μ_{on} showed that there is always a starting vortex, but jet is the dominant flow (Gharib et al. 1998, established this to be the case for $U_J\mu_{\mathrm{on}}/D_J \gtrsim 4$). Thus, we recommend $U_J\mu_{\mathrm{on}}/D_J \approx 4$ as the lower bound for selecting the mean on-time. The far-field measurements of an individual pulsed jet showed that the momentum of the fluid set into motion diffuses and thus the peak velocity measured at the tank center is smaller compared to a continuous jet. However, as the on-time increases, the velocity of a pulsed jet recovers to the continuous jet value for $U_J\mu_{\mathrm{on}}/(\frac{1}{2}L_A) \gtrsim 4$. Increasing the on-time beyond this value does not provide a further increase in jet velocity at the tank center, but produces a peak at the forcing timescale in the velocity spectra. Thus, we recommend that $\mu_{\mathrm{on}}U_J/(\frac{1}{2}L_A) \approx 4$ be used as the upper bound for selecting the mean on-time.

Acknowledgements We thank Luke Summey for help with tank design and construction, and Evan Variano, Gautier Verhille, and Greg Voth for useful discussions. We would also like to thank the anonymous referees whose comments and suggestions helped to improve the paper considerably.

Author contributions All authors contributed to the study conception, design, execution, and writing. Material preparation, data collection, and analysis were led by Joo Young Bang. The first draft of the manuscript was written by Joo Young Bang, and all authors subsequently edited the manuscript. All authors read and approved the final manuscript.

Funding We gratefully acknowledge support from the US National Science Foundation (CBET-2211704).

Availability of data and materials All data and materials are available upon request and are being prepared to be posted on a webserver

Declarations

Conflict of interest Not applicable.

Ethical approval Not applicable.

References

Adrian RJ, Westerweel J (2011) Particle image velocimetry. Cambridge University Press, Cambridge

Bellani G, Variano EA (2013) Homogeneity and isotropy in a laboratory turbulent flow. Exp Fluids 55:1646. https://doi.org/10.1007/s00348-013-1646-8

Birouk M, Chauveau C, Sarh B, Quilgars A, Gökalp I (1996) Turbulence effects on the vaporization of monocomponent single droplets. Combust Sci Technol 113(1):413–428. https://doi.org/10.1080/00102209608935506

Blum DB, Kunwar SB, Johnson J, Voth GA (2010) Effects of nonuniversal large scales on conditional structure functions in turbulence. Phys Fluids 22:015107. https://doi.org/10.1063/1.3292010

Bounoua S, Bouchet G, Verhille G (2018) Tumbling of inertial fibers in turbulence. Phys Rev Lett. https://doi.org/10.1103/physrevlett.121.124502

Brunk B, Weber-Shirk M, Jensen A, Jirka G, Lion LW (1996) Modeling natural hydrodynamic systems with a differential-turbulence column. J Hydraul Eng 122:373–380. https://doi.org/10.1061/(asce)0733-9429(1996)122:7(373)

Carter D, Petersen A, Amili O, Coletti F (2016) Generating and controlling homogeneous air turbulence using random jet arrays. Exp Fluids. https://doi.org/10.1007/s00348-016-2281-y

Chang K, Bewley GP, Bodenschatz E (2012) Experimental study of the influence of anisotropy on the inertial scales of turbulence. J Fluid Mech 692:464–481. https://doi.org/10.1017/jfm.2011.529

Davidson P (2015) Turbulence. Oxford University Press, Oxford. https://doi.org/10.1093/acprof:oso/9780198722588.001.0001

De Jong J, Cao L, Woodward S, Salazar J, Collins L, Meng H (2009) Dissipation rate estimation from PIV in zero-mean isotropic turbulence. Exp Fluids 46:499–515. https://doi.org/10.1007/s00348-008-0576-3

Dou Z, Pecenak ZK, Cao L, Woodward SH, Liang Z, Meng H (2016) PIV measurement of high-Reynolds-number homogeneous and isotropic turbulence in an enclosed flow apparatus with fan agitation. Meas Sci Technol 27:035305. https://doi.org/10.1088/0957-0233/27/3/035305

Douady S, Couder Y, Brachet ME (1991) Direct observation of the intermittency of intense vorticity filaments in turbulence. Phys Rev Lett 67:983–986. https://doi.org/10.1103/physrevlett.67.983

Esteban LB, Shrimpton JS, Ganapathisubramani B (2019) Laboratory experiments on the temporal decay of homogeneous anisotropic turbulence. J Fluid Mech 862:99–127. https://doi.org/10.1017/jfm.2018.964

Fernando HJS, De Silva IPD (1993) Note on secondary flows in oscillating-grid, mixing-box experiments. Phys Fluids A 5:1849–1851. https://doi.org/10.1063/1.858808

Frisch U (1995) Turbulence: the legacy of a. n. kolmogorov. https://doi.org/10.1017/cbo9781139170666

Gao L, Yu SCM (2010) A model for the pinch-off process of the leading vortex ring in a starting jet. J Fluid Mech 656:205–222. https://doi.org/10.1017/S0022112010001138

Gharib M, Rambod E, Shariff K (1998) A universal time scale for vortex ring formation. J Fluid Mech 360:121–140. https://doi.org/10.1017/S0022112097008410

Goepfert C, Marié J-L, Chareyron D, Lance M (2009) Characterization of a system generating a homogeneous isotropic turbulence field by free synthetic jets. Exp Fluids 48:809–822. https://doi.org/10.1007/s00348-009-0768-5

Guo Y, Malcangio D, Davies PA, Fernando HJS (2005) A laboratory investigation into the influence of a localized region of turbulence on the evolution of a round turbulent jet. Fluid Dyn Res 36:75. https://doi.org/10.1016/j.fluiddyn.2005.01.001

Hoffman DW, Eaton JK (2021) Isotropic turbulence apparatus with a large vertical extent. Exp Fluids. https://doi.org/10.1007/s00348-021-03311-7

Hwang W, Eaton JK (2004) Creating homogeneous and isotropic turbulence without a mean flow. Exp Fluids 36:444–454. https://doi.org/10.1007/s00348-003-0742-6

Ishihara T, Gotoh T, Kaneda Y (2009) Study of high–reynolds number isotropic turbulence by direct numerical simulation. Annu Rev Fluid Mech 41:165–180. https://doi.org/10.1146/annurev.fluid.010908.165203

Johnson BA, Cowen EA (2018) Turbulent boundary layers absent mean shear. J Fluid Mech 835:217–251. https://doi.org/10.1017/jfm.2017.742

Johnson BA, Cowen EA (2020) Sediment suspension and bed morphology in a mean shear free turbulent boundary layer. J Fluid Mech 894:A8. https://doi.org/10.1017/jfm.2020.222

Khorsandi B, Gaskin S, Mydlarski L (2013) Effect of background turbulence on an axisymmetric turbulent jet. J Fluid Mech 736:250–286. https://doi.org/10.1017/jfm.2013.465

Lawson JM, Dawson JR (2015) On velocity gradient dynamics and turbulent structure. J Fluid Mech 780:60–98. https://doi.org/10.1017/jfm.2015.452

Lawson JM, Ganapathisubramani B (2021) Unsteady forcing of turbulence by a randomly actuated impeller array. Exp Fluids. https://doi.org/10.1007/s00348-021-03364-8

Moisy F, Tabeling P, Willaime H (1999) Kolmogorov equation in a fully developed turbulence experiment. Phys Rev Lett 82:3994–3997. https://doi.org/10.1103/PhysRevLett.82.3994

Mydlarski L, Warhaft Z (1998) Passive scalar statistics in high-péclet-number grid turbulence. J Fluid Mech 358:135–175. https://doi.org/10.1017/s0022112097008161

Pérez-Alvarado A, Mydlarski L, Gaskin S (2016) Effect of the driving algorithm on the turbulence generated by a random jet array. Exp Fluids. https://doi.org/10.1007/s00348-015-2103-7

Pope SB (2000) Turbulent flows. Cambridge University Press, Cambridge

Poulain-Zarcos M, Mercier MJ, ter Halle A (2022) Global characterization of oscillating grid turbulence in homogeneous and two-layer fluids, and its implication for mixing at high Peclet number. Phys Rev Fluids. https://doi.org/10.1103/physrevfluids.7.054606

Pujara N, Clos KTD, Ayres S, Variano EA, Karp-Boss L (2021) Measurements of trajectories and spatial distributions of diatoms (*coscinodiscus* spp.) at dissipation scales of turbulence. Exp Fluids. https://doi.org/10.1007/s00348-021-03240-5

Rensen J, Luther S, Lohse D (2005) The effect of bubbles on developed turbulence. J Fluid Mech 538:153. https://doi.org/10.1017/s0022112005005276

Roy S, Acharya S (2012) Scalar mixing in a turbulent stirred tank with pitched blade turbine: role of impeller speed perturbation. Chem Eng Res Des 90(7):884–898. https://doi.org/10.1016/j.cherd.2011.10.009

Saarenrinne P, Piirto M, Eloranta H (2001) Experiences of turbulence measurement with PIV*. Meas Sci Technol 12:1904. https://doi.org/10.1088/0957-0233/12/11/320

Sahebjam R, Kohan KF, Gaskin S (2022) The dynamics of an axisymmetric turbulent jet in ambient turbulence interpreted from the passive scalar field statistics. Phys Fluids 34:015129. https://doi.org/10.1063/5.0071023

Schram C, Riethmuller ML (2001) Vortex ring evolution in an impulsively started jet using digital particle image velocimetry and continuous wavelet analysis. Meas Sci Technol 12(9):1413. https://doi.org/10.1088/0957-0233/12/9/306

Silva IPDD, Fernando HJS (1994) Oscillating grids as a source of nearly isotropic turbulence. Phys Fluids 6:2455–2464. https://doi.org/10.1063/1.868193

Tan S, Xu X, Qi Y, Ni R (2023) Scalings and decay of homogeneous, nearly isotropic turbulence behind a jet array. Phys Rev Fluids 8:024603. https://doi.org/10.1103/PhysRevFluids.8.024603

Variano EA, Cowen EA (2008) A random-jet-stirred turbulence tank. J Fluid Mech 604:1–32. https://doi.org/10.1017/S0022112008000645

Variano EA, Cowen EA (2013) Turbulent transport of a high-schmidt-number scalar near an air-water interface. J Fluid Mech 731:259–287. https://doi.org/10.1017/jfm.2013.273

Variano EA, Bodenschatz E, Cowen EA (2004) A random synthetic jet array driven turbulence tank. Exp Fluids 37:613–615. https://doi.org/10.1007/s00348-004-0833-z

Veeravalli S, Warhaft Z (1989) The shearless turbulence mixing layer. J Fluid Mech 207:191–229. https://doi.org/10.1017/S0022112089002557

Voth GA, Satyanarayan K, Bodenschatz E (1998) Lagrangian acceleration measurements at large reynolds numbers. Phys Fluids 10:2268–2280. https://doi.org/10.1063/1.869748

Voth GA, La Porta A, Crawford AM, Alexander J, Bodenschatz E (2002) Measurement of particle accelerations in fully developed turbulence. J Fluid Mech 469:121–160. https://doi.org/10.1017/S0022112002001842

Worth NA, Nickels TB (2011) Time-resolved volumetric measurement of fine-scale coherent structures in turbulence. Phys Rev E. https://doi.org/10.1103/physreve.84.025301

Yamamoto K, Watanabe T, Nagata K (2022) Turbulence generated by an array of opposed piston-driven synthetic jet actuators. Exp Fluids 63:35. https://doi.org/10.1007/s00348-021-03351-z

Zimmermann R, Xu H, Gasteuil Y, Bourgoin M, Volk R, Pinton J-F, Bodenschatz E, I. C. for Turbulence Research (2010) The Lagrangian exploration module: an apparatus for the study of statistically homogeneous and isotropic turbulence. Rev Sci Inst, 81:055112. https://doi.org/10.1063/1.3428738